UPPSALA
UNIVERSITET

Digital Comprehensive Summaries of Uppsala Dissertations from the Faculty of Science and Technology 1972

Towards quinone/pEDOT conducting redox polymers as energy storage materials

HUAN WANG

ACTA
UNIVERSITATIS
UPSALIENSIS
UPPSALA
2020

ISSN 1651-6214
ISBN 978-91-513-1021-3
urn:nbn:se:uu:diva-419470

Dissertation presented at Uppsala University to be publicly examined in Siegbahnsalen, 10101, Ångström, Lägerhyddsvägen 1, Uppsala, Monday, 23 November 2020 at 13:15 for the degree of Doctor of Philosophy. The examination will be conducted in English. Faculty examiner: Professor Xavier Crispin (Linköping University).

Abstract
Wang, H. 2020. Towards quinone/pEDOT conducting redox polymers as energy storage materials. *Digital Comprehensive Summaries of Uppsala Dissertations from the Faculty of Science and Technology* 1972. 79 pp. Uppsala: Acta Universitatis Upsaliensis.
ISBN 978-91-513-1021-3.

With the increased demand for electrical energy storage devices, *e.g.* electric vehicles and smart grids, organic batteries have caught increasing attention due to their advantages, such as sustainability, environmental friendliness and cheap raw materials over traditional inorganic energy storage materials. Quinones, as an organic energy storage materials have high specific capacity, show fast $2e^-$ redox reactions and provide a wide structural diversity, making them promising candidates as active battery materials. However, quinones often suffer from dissolution problem and limited electronic conductance. In this thesis, quinones are functionalized onto conducting polymer backbones to make a conducting redox polymer (CRP), where the quinone provides capacity while the conducting polymer backbone provides electronic conductance and prevents dissolution of the quinone. One fundamental requirement to make a functional CRP is that redox matching between the quinone redox potential and the conducting region of the conducting polymer is achieved. To that end, the quinone redox chemistry as well as the conductance behavior of conducting polymers must be fully understood. In this thesis, the quinone redox chemistry was firstly studied, regarding the effect of cycling cation, solvent and substituent. In this thesis, the effect of cycling cation, solvent and substitution on the quinone redox chemistry was studied and found to systematicall

y tune the quinone redox potential, with the nature of the cycling ion showing the largest effect. Quinones were covalently attached onto 3,4-ethylenedioxythiophene (EDOT) and polymerized, the obtained CRPs were characterized. It was found that a doping threshold was required before an appreciable conductance was observed, causing a conductance delay and the loss of redox matching. *In situ* EQCM, *in situ* UV-vis and *in situ* EPR showed that the conductance delay was attributed to the localization of charge carriers in the CRPs as a result of the interaction between the pEDOT backbone and the reduced, lithiated quinone state. The redox matching was improved by the utilization of a high potential quinziarin. A quinizarin-CRP based lithium ion battery (LIB) was fabricated that showed improved stability compared to that of the quinone based CRP. In addition, an all CRP based organic proton battery using the quinizarin-CRP as cathode and naphthoquinone-CRP as anode was developed. Lastly, a post-deposition polymerization (PDP) method was developed and the polymerization mechanism was investigated.

Keywords: quinone, conducting redox polymer, doping, capacity, organic battery, polymerization

Huan Wang, Department of Materials Science and Engineering, Nanotechnology and Functional Materials, Box 534, Uppsala University, SE-751 21 Uppsala, Sweden.

ISSN 1651-6214
ISBN 978-91-513-1021-3
urn:nbn:se:uu:diva-419470 (http://urn.kb.se/resolve?urn=urn:nbn:se:uu:diva-419470)

Forever love

To my family

List of papers

This thesis is based on the following papers, which are referred to in the text by Roman numerals.

I Wang H., Emanuelsson R., Banerjee A., Ahuja R., Strømme M., and Sjödin M. . *Journal of Physical Chemistry C*, 2020, 124, 13609−13617.

II Wang H., Emanuelsson R., Liu H.D., Kristina E., Mamedov F., Strømme M., and Sjödin M. Redox-State-Dependent Interplay between Pendant Group and Conducting Polymer Backbone in Quinone-Based Conducting Redox Polymers for Lithium Ion Batteries. *ACS Applied Energy Materials*. 2019, 2, 7162−7170

III Wang H., Emanuelsson R. Liu H.D., Strømme M., and Sjödin M. A conducting additive-free high potential quinone based lithium ion battery cathode. *In manuscript*.

IV Wang H., Emanuelsson R. Strømme M., and Sjödin M. Unrevealing the post-deposition electrochemical polymerization mechanism and the fabrication of a conducting additive-free all organic rocking chair proton battery. *In manuscript.*

My contribution to the included papers

Paper I: I participated in the planning of the study and performed all the experiments except for the synthesis of organic molecules and DFT calculations. I carried out all the data analysis, wrote the initial manuscript and contributed to the continued writing process.

Paper II: I participated in the planning of the study and performed all the experiments except for the synthesis of monomers and battery fabrication. I carried out all the data analysis, wrote the initial manuscript and contributed to the continued writing process.

Paper III: I participated in the planning of the study and performed all the experiments except for the synthesis of trimers and battery fabrication. I carried out all the data analysis, wrote the initial manuscript and contributed to the continued writing process.

Paper IV: I participated in the planning of the study and performed all the experiments except for the synthesis of trimers. I carried out all the data analysis, wrote the initial manuscript and contributed to the continued writing process.

Contents

Abbreviations

LIB	Lithium ion battery
CRPs	Conducting redox polymers
MeCN	Acetonitrile
NMP	N-Methyl-2-pyrrolidone
pEDOT	Poly(3,4-ethylenedioxythiophene)
Q	Quinone
Qz	Quinizarin
NQ	Naphthoquinone
CV	Cyclic voltammetry
WE	Working electrode
RE	Reference electrode
CE	Counter electrode
GC	Glassy carbon
Fc	Ferrocene
$TBAPF_6$	Tetrabutylammonium hexafluorophosphate
OCP	Open circuit potential
CB	Conduction band
VB	Valance band
EQCM	Electrochemical quartz crystal microbalance
UV-vis	Ultraviolet-visible
PDP	Post-deposition electrochemical polymerization

Symbols

Symbol	**name**	**unit**
A	Area	m^2
C	Concentration	mol m^{-3}
D	Diffusion coefficient	m^2 s^{-1}
E^0	Standard potential	V
$E^{0'}$	Formal potential	V
R	Gas constant	J mol^{-1} K^{-1}
m	Mass	kg
λ	Wavelength	nm

1. General introduction

With the over-exploitation of limited natural resources such as oil and gas, energy supply has become a global challenge, requiring a change of the present energy structure. Battery, as an energy storage technique, can effectively reduce the strong dependence of industry on oil and gas. Up to now, lithium ion batteries (LIB), as the most popular electrical energy storage devices, however, suffer from i) limited availability of raw materials, which currently rely on inorganic materials (Co, Fe, Mn, Ni); ii) negative environmental impact during manufacturing, for example, high CO_2 footprint, and iii) poor safety.[1–3] It is therefore desirable to find alternative materials that are eco-friendly, abundant and safe. Organic batteries (containing C, H, O, N) are currently being widely investigated because of their potentially sustainable life cycle, the availability of their building blocks, low price and the various possibilities for tuning the material properties to meet specific end-user needs through molecular engineering. However, small, high-capacity organic molecules suffer from intrinsic dissolution problem as well as limited electronic conductivity. Conducting polymers, on the other hand, are potentially conducting. However, they suffer from low capacity and an undefined redox potential due to the potential-dependent doping/dedoping mechanism for charge storage. These issues can be overcome by attaching redox-active molecules onto a polymer backbone, forming a conducting redox polymer (CRPs). The polymer backbone provides conductance as well as prevents dissolution of the organic molecules while the organic molecules provide capacity and a well-defined redox potential. The CRP concept thus eliminates the dependence on conducting additives. The basic requirement to make a functional CRP is redox matching between the formal potential of redox-active molecule and the conducting region of the polymer backbone. Since conducting polymers are only conducting in certain potential region and the redox potential of the organic molecules must be within this region.

In this thesis, the redox chemistry of quinones, with particular focus on the effects of the charge compensating cation, solvent and substituent, were studied to explore the possibility to use quinone as pendant group to develop redox matched CRP with a pEDOT-based conducting polymer backbone. Two LIBs using CRP based cathodes were fabricated to study the electrochemical performance of the CRPs in batteries. An all CRPs based rocking-chair proton battery was also fabricated.

2. Aims of the thesis

The final aim of the thesis is to use pEDOT-based polymer as conducting backbone to design stable quinone-based battery electrodes using the CRP strategy. High performance CRP relies on the exertion of both conducting property of polymer backbone and the redox activity of quinone. This was achieved through the fundamental study of quinone redox chemistry to give guidelines to the CRP-design. The fundamental study on conducting mechanism of CRPs then provides further CRP-design criteria.

The specific aims of these works are described as follows:

- To explore the fundamental quinone redox chemistry and how it is affected by factors such as charge-compensating cation, solvent and substituents (**Paper I**)
- To study the doping and conducting mechanism of CRPs (**Paper II**)
- To study the redox matching between the quinone redox potential and the conducting region of the conducting polymer backbone, as well as its effect on the stability of the resulting CRPs cathode (**Paper II and III**)
- To understand the polymerization mechanism during PDP process (**Paper IV**)
- To use CRPs as active materials in both the cathode and the anode in an all organic proton battery (**Paper IV**)

3. Electrochemical methods and techniques

3.1 Electrochemical methods

Electrochemical methods comprise various methods to monitor the electrochemical response of an analyte in an electrochemical cell. The cell can either be a three-electrode setup or a two-electrode setup and the analyte can either be dissolved in electrolyte, or a solid film immobilized onto the electrode.

3.1.1 Electrochemical cell setup

In term of the cell category, the cell can be a three-electrode setup or a two-electrode setup. In a three-electrode setup, the three electrodes are a counter electrode (CE), a working electrode (WE) and a reference electrode (RE). The WE is involved in two separate circuits, namely the current circuit together with the CE to monitor current flow on the WE and potential circuit together with the RE to monitor potential on the WE. The CE is used to balance the charge from WE, the current in the electrolyte is sustained by ion movement while the current in the electrical circuit is sustained by electrons. The current on the WE could either result from electron-transfer produced faradaic current or double layer charging produced capacitive current. The amount of charge produced or consumed on the WE must be exactly balanced by the inert CE. This is accomplished by oxidation/reduction of the solvent or electrolyte on CE. A separate compartment for the CE is usually used to prevent the byproducts from the side reactions on CE to reach the WE. A porous frit allows for ion motion between the two compartments. The RE is used to control the potential of the WE. The redox couple (Ag^+/Ag^0) with a defined potential, kept in a separated compartment, is used as RE in this thesis. To fully avoid the leakage of Ag^+ from the reference electrolyte solution into the investigated electrochemical cell, an additional compartment is used for the RE. In order to have a well-defined potential standard, the RE is calibrated against the ferrocene redox couple (Fc^+/Fc^0) after each experiment and the potential is reported against Fc^+/Fc^0 in this thesis. The CE is a platinum wire (Pt) and the WE is glassy carbon (GC) unless otherwise specified.

In practical applications, *e.g.* batteries, fuel cells, and supercapacitors, two-electrode setups are used, namely cathode and anode. The anode balances the charge on the cathode as well as provides a reference potential. The voltage is

determined by the potential difference between the two electrodes. In LIBs, Li metal is used as anode. The defined redox potential of Li^+/Li^0 (-3.0 V vs. SHE) gives a stable reference potential, the battery voltage output is thus associated with the cathode potential.

3.1.2 Cyclic voltammetry

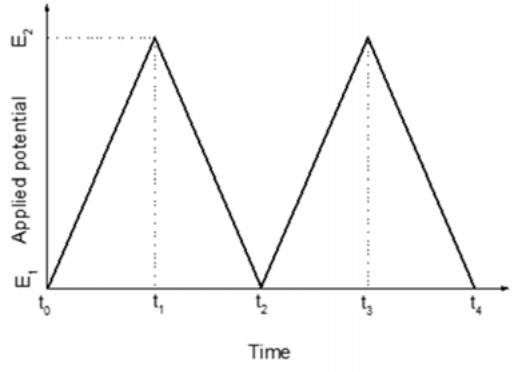

Figure 1. Potential waveform in cyclic voltammetry method.

Electrochemical methods are divided into several categories depending on the controlled parameter. In this thesis cyclic voltammetry (CV) is the most commonly used electrochemical method, providing a direct way to visualize the current response as a function of potential. In CV, the applied potential on the WE increases linearly with time during the anodic scan (Figure 1). After the potential reaches the predefined upper limit E_2, the potential then decreases linearly with time to the predefined lower limit E_1 during the cathodic scan. The speed at which the potential varies is called scan rate. During this process, the current response of the analyte is recorded as a function of the applied potential. The analyte could be either dissolved in the electrolyte or immobilized onto the current collector. In this thesis, both situations were investigated.

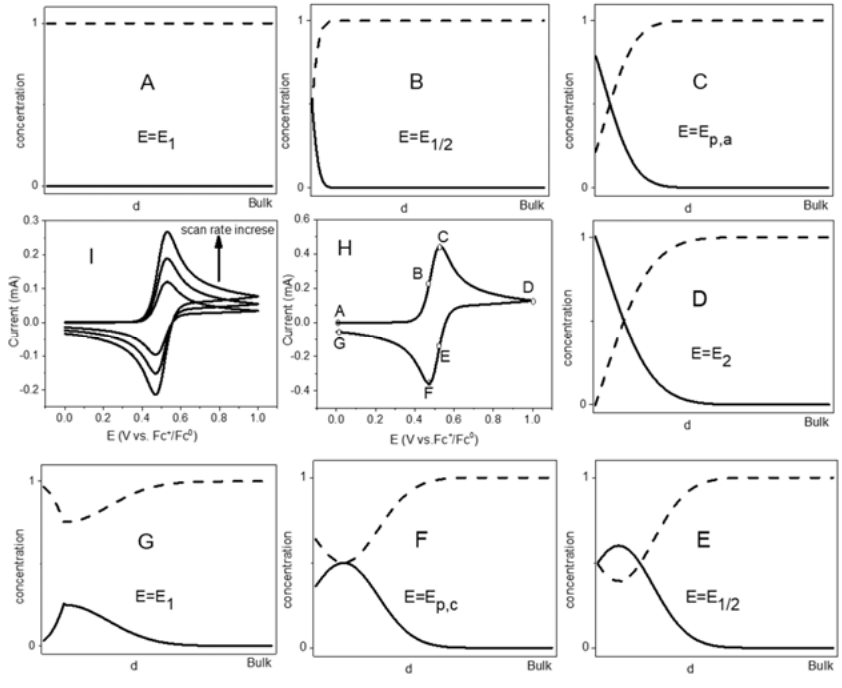

Figure 2. Typical cyclic voltammograms of dissolved, initially reduced analyte (H), concentration gradient of reduced state (dashed line) and oxidized state (solid line) in diffusion layer at the point of A, B, C, D in the anodic scan; at the point of E, F, G in the cathodic scan. Cyclic voltammograms of dissolved analyte at different scan rates (I)

In the case of a dissolved analyte, the redox reaction is usually limited by the diffusion of analyte to the electrode surface.[4] Figure 2H shows the cyclic voltammograms of dissolved reduced species as initial analyte. At point A, the concentration of reduced species (c_{re}) around the electrode surface is 1 and concentration of oxidized species (c_{ox}) is 0. As the potential increases in the anodic scan, the oxidation process proceeds and the reduced species at the electrode surface are oxidized to oxidized species, thus c_{re} decreases and c_{ox} increases at the electrode surface. The redox reaction at the surface builds up a concentration gradient as the surface concentration, given by the Nernst equation (eq 1), differs from the concentration in the bulk solution:

$$E_{red} = E_{red}^{o'} - \frac{RT}{zF} \times ln \frac{\alpha_{red}}{\alpha_{ox}} \quad (1)$$

In eq (1) α is the chemical activity for the relevant species, z is the number of electrons transferred per formula unit, F is faradic constant (96485 C/mol), R is gas constant (8.314 J/mol·K), T is temperature (K) and $E^{0'}$ is the formal potential.

The existence of the concentration gradient produces a flux that goes from the high concentration region to the low concentration region with a magnitude that is proportional to the concentration gradient according to Fick's first law. The existence of the concentration gradient also produces a diffusion layer at the electrode surface which is on the micrometer length-scale. In the diffusion layer, c_{ox} is high at the electrode surface and decreases with the distance from the electrode surface, while c_{re} is low at the electrode surface and increases with the distance from the electrode surface. In the bulk solution, c_{re} is always 1 while c_{ox} is always 0.

At point B in Figure 2H, the applied potential E is equal to formal potential ($E_{1/2}$) of the redox reaction, therefore $c_{re}=c_{ox}$ at the surface. At point C, the net flux of the two redox species reaches the maximum value, giving the maximum anodic current. At point D, the positive scan reaches the set potential limit, $c_{re} = 0$ and $c_{ox} = 1$ at the electrode interface. However, the continuous flux of reduced species from the bulk solution to the electrode surface produces the infinite diffusion current tail in cyclic voltammograms. As long as the diffusion layer exists, the current at the set potential limit will never decline to zero, a so-called diffusion tail is observed.

In the reverse cathodic scan, the oxidized species at the electrode surface is firstly reduced, causing the decline of c_{ox} and increase of c_{re} at the electrode surface. At E point, $c_{re}= c_{ox.}$ At point F, the net flux of oxidized species to the electrode surface and reduced species to the bulk solution reaches a maximum value, producing a maximum negative cathodic current. At point G the oxidized species at the electrode surface is limited, further reduction causes the flux of the residual oxidized species from the diffusion layer to the electrode surface, producing a negative current tail. Unlike the diffusion layer at point D, where endless amounts of reduced species exist in the bulk and the current diffusion tail never disappear. The diffusion current tail in the cathodic scan may disappear after sufficient reduction time. Worth to note is that a lower scan rate allows more time for the diffusion layer to grow further from the electrode (Figure 2I).

In the diffusion-controlled system, the electron transfer rate at the electrode surface is sufficiently fast to ensure that equilibrium is established close to the electrode surface at all times during the experiment. In the special situation ($D_{Ox} = D_{Red}$):

1) The anodic peak current is equal to the cathodic peak current after the subtraction of background current.
2) The position of anodic and cathodic peak does not alter with the scan rate.
3) The anodic and cathodic peak separation is 56/n eV, where n is electron transfer number for the electrode redox reaction. The theoretical peak split is 56 mV for 1e transfer process and 28 mV for 2e transfer process.

4) The observed peak current is proportional to the square root of the scan rate ($v^{1/2}$) according to Randles-Sevcik equation:[5,6]

$$I_p = (2.69\times10^5)\, n^{3/2} A\, D_0^{1/2} Co^* v^{1/2} \quad (2)$$

where D (cm^2s^{-1}) is the diffusion coefficient of analyte in the electrolyte, Co* (mol cm^{-3}) is the initial concentration of analyte in the electrolyte, n is the electron transfer number, and A (cm^2) is active area of the WE.

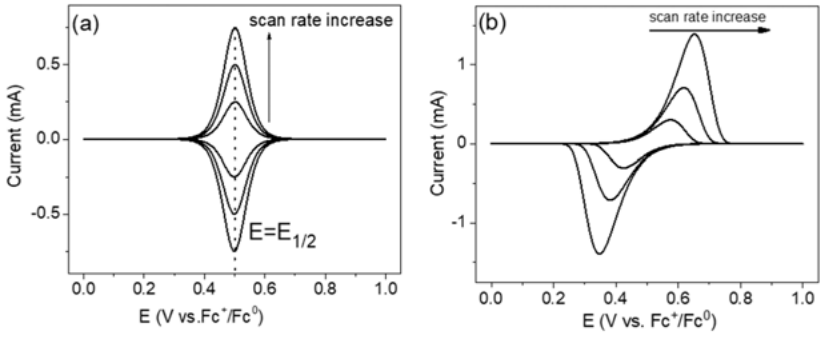

Figure 3. Cyclic voltammograms of (a) thermoldynamic controlled system, (b) kinetic controlled system at different scan rates

For the situation where the analyte is immobilized onto the current collector the redox reaction is governed by three possible processes depending on the rate-limiting process. One is thermodynamic-control, where all processes involved in the redox conversion *e.g.* ion diffusion in the electrolyte and in the diffusion layer, electron transfer and electron transport are faster compared to the applied voltage change. In this case the cyclic voltammograms shows a pair of sharp redox peaks. Both the anodic peak and the cathodic peak are exactly located at the standard potential with a peak separation of 0 mV (Figure 3a). The peak separation (0 mV) does not change with the scan rate, whereas the peak current is proportional to scan rate according to equation (3):[7]

$$I_p=(9.39\times10^5)\, n^2 A \Gamma v \quad (3)$$

Where Γ (mol cm^2) is the surface coverage of the analyte; n, A and *v* have the same meaning as that in equation (2). In this situation, counter ions involved in the redox reaction have sufficiently high diffusion coefficient.

The redox reaction of immobilized analyte can also be kinetically controlled, where the electrode electron transfer is slower compared to the applied potential change. In this case the current requires more time to respond to the applied voltage, causing a non-equilibrium state where the Nernst equation is not valid. In this case the surface concentration cannot be predicted by the

Nernst equation. Thus, the slow electron transfer rate causes a shift of the peak position. A peak separation between the anodic and cathodic peaks is observed and the separation increases with scan rate (Figure 3b). When the peak potential has moved sufficiently far from the formal potential the Laviron treatment can be applied to calculate the average rate constant:[8]

$$E_p = E^{0'} \pm \frac{RT}{\alpha zF} \times ln(\frac{\alpha zFv}{RTk^0}) \quad (4)$$

where α is the transfer coefficient, z is the number of charges transferred, k^0 is rate constant (s^{-1}), v is scan rate (V/s) , $E^{0'}$ is the formal potential, where the plus sign signifies reduction and the minus sign signifies oxidation. The peak separation increases with the decreased rate constant as well as the increased scan rate.

The redox reaction of immobilized analyte can also be controlled by diffusion like that in the dissolved analyte situation. Again, the peak separation is theoretically expected to be constant at 56 mV for 1e reaction and at 28 mV for 2e reaction, the peak current is proportional to $v^{1/2}$ according to equation (2). Cyclic voltammograms are expected to show a diffusion tail. The slow diffusion could be explained by the slow electron hoping rate due to low conductivity, as well as slow counter ion transport within the immobilized analyte layer.

For both dissolved analyte and immobilized analyte, diffusion-controlled systems always have a diffusion tail as a characteristic. The diffusion tail indicates that the full redox conversion of analyte cannot be achieved due to the concentration gradients in solution near the electrode (dissolved analyte system) or within the analyte layer (analyte immobilized onto the electrode surface). The rate-limiting steps described above are under ideal conditions. In practical situation the CV is more complex than the ideal situation, due to the binary effects of polarization as well as intricate diffusion geometries. In addition, in some cases the diffusion and electron transfer is equally slow on time-scale and both are the rate-limiting step. The obtained cyclic voltammograms might be different from the ideal cases regarding peak separation and peak broadness.

In this thesis, all investigated systems with conducting polymers immobilized onto electrode are thermodynamically controlled at low scan rate with peak currents directly proportional to the scan rate. At high scan rate, the systems are kinetically controlled and the peak separation increases with scan rate. There is no diffusion tail even at high scan rates and hence all the redox species can be converted.

3.1.3 Square wave voltammetry

Square wave voltammetry is a form of linear potential sweep voltammetry, where a combination of square wave and staircase potential is applied to a stationary electrode. Compared with CV, this technique can effectively suppress the non-faradaic background current contribution to the overall current signal. The background current could be non-faradaic current. In this thesis, square wave voltammetry is used to determine the formal potential of dissolved analytes in solution, as a compliment method to CV as high sensitivity is needed when the analyte concentration is low.

3.1.4 Chronoamperometry method

In contrast to CV measurement where the applied potential varies linearly with time and the current response is recorded as a function of potential. The chronoamperometry method is based on stepwise potential change and the current response is recorded as a function of time. In this thesis, this method is mainly used to reach the equilibrium state at a certain potential rapidly, as well as for charging a battery completely.

3.2 *In* situ electrochemical techniques

In situ refers to recording changes in *e.g.* mass, conductance, spin and spectra properties during operation of the electrochemical techniques. By utilizing *in situ* techniques, direct measurements at specific potentials can be conducted. Conversely, *ex situ* experiments are performed in the absence of potential control.

3.2.1 *In situ* UV-vis spectroscopy

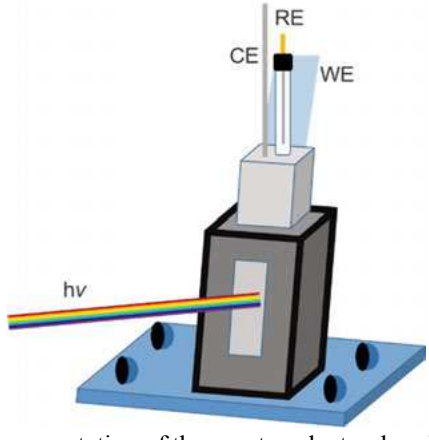

Figure 4. Schematic representation of the spectro-electrochemical cell for *in situ* UV-vis measurement.

In molecules, electrons in the low energy states can be excited to high energy states upon absorbing a photon in the form of ultraviolet or visible light. The energy gap between the two states determines the photon energy that the excitation requires: the smaller the gap, the higher wavelength of the photon. *In situ* UV-vis spectroscopy is the combination of UV-vis spectroscopy and electrochemistry techniques. Spectral changes of redox-active species is recorded as a function of applied potential.[9] The redox-active molecules could either be solid layers or dissolved species. In this thesis, the spectro-electrochemistry of electroactive solid layers was investigated. Spectro-electrochemical measurements are commonly made in a liquid cell with a large electrolyte reservoir. The WE is commonly a conductive Indium tin oxide (ITO), of which part is put in the beam path while the other side is above the electrolyte and connected to the outer circuit (Figure 4). The CE and the RE are positioned above the light path and immersed into the electrolyte. In this thesis, conducting polymers were electrochemically polymerized onto ITO glass and the polymer doping process was studied in terms of the absorbance evolution of the bandgap transition and transitions originating from the produced intra bandgap states upon doping.

3.2.2 *In situ* ATR-FTIR

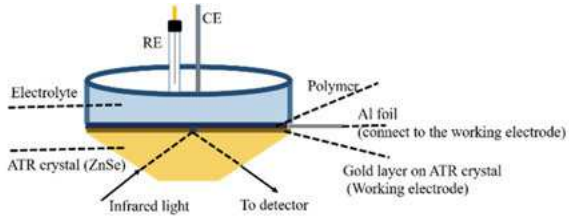

Figure 5. Schematic representation of the spectro-electrochemical cell for *In situ* FTIR measurement.

Molecules can absorb infrared light with a resonant frequency that matches the vibrational energy of a certain bond in the molecule. The resonant frequency is characteristic of certain bond structure in a specific environment. The energy is determined by the characteristic force constant of the bond and the mass of the atoms in the bond. The energy of the bond can also be affected by vibronic coupling with the neighboring atoms. In attenuated total reflection-fourier transform infrared spectroscopy FTIR (ATR-FTIR) set-up, the infrared light beam is directed onto a ZnSe crystal with high refractive index. The investigated organic film was coated on the surface of ZnSe crystal which was pre-coated by a conductive layer on the top surface. When the beam of infrared light is internally directed into the ZnSe crystal and undergoes internal reflections within the crystal, evanescent wave is produced at the crystal-sample interface. The evanescent wave can extend into the investigated film.

To investigate the evolution of certain characteristic bond in organic molecules upon oxidation or reduction, ATR-FTIR in combination with electrochemical technique is used, a method here called *in situ* ATR-FTIR. In this thesis, a gold-coated (around 10 nm in thickness) ZnSe crystal was used as WE. The trimer was coated and electrochemically polymerized onto the gold surface in a three-electrode setup with CE and RE above the ZnSe crystal (Figure 5). The vibrational absorption change of carbonyl bond in the resulting polymer upon reduction/oxidation was studied.

3.2.3 *In situ* Electrochemical Quartz Crystal Microbalance measurement

Mechanical stress applied to some materials (notably crystals, certain ceramics) can cause the shift of positive and negative charge centers within the crystal. The charge separation produces an external electrical field, which is called piezoelectric effect. The principle of the Quartz Crystal Microbalance (QCM) is based on the reverse piezoelectric effect, where an alternating current applied on the crystal can cause a mechanical deformation (motion) within the quartz crystal. The mechanical deformation frequency is dependent on the

elastic properties of the crystal, which are in turn affected by the mass of material coated on the crystal.

In Electrochemical Quartz Crystal Microbalance measurement (EQCM), the resonant frequency change of the crystal upon an electrochemical reaction is measured. According to the Sauerbrey equation (eq. 5) the resonance frequency can be quantitatively converted to the mass change of the material coated on the crystal:[10]

$$\Delta f = -\frac{2 f_0^2}{\sqrt{u_q p_q}} \frac{\Delta m}{A} \tag{5}$$

where Δf (Hz) is the measured frequency change, f_0 is the resonant frequency of the quartz crystal, which is 9 MHz for a gold-coated quartz QCM crystal in this thesis, Δm is the mass change on the quartz crystal, A is the piezoelectrically active area (0.198 cm^2), u_q is the AT-cut quartz constant ($2.947*10^{11}$ g $cm^{-1}s^{-2}$), and p_q is the quartz crystal density (2.65 g cm^{-2}).

The Sauerbrey equation assumes a rigid film that has the same acoustic properties as the crystal and that the frequency change is small ($\Delta f / f_0 < 0.05$). In this thesis, a thin polymer is electrochemically polymerized uniformly onto the gold coated quartz WE, which was connected to an external-sensor to record the frequency change during electrochemical processes. The WE is positioned at the bottom of the cell while CE and RE are positioned above WE (Figure 6). The EQCM method was used to determine the polymer mass deposited on the electrode surface during electrochemical polymerization from a monomer solution, as well as the solvent uptake during post-deposition polymerization (PDP). In addition, mass change caused by counter cation uptake or expulsion during pendant redox reaction, as well as the polymer backbone doping induced counter anion uptake were investigated. The mass change per molar charge in a certain potential region can be calculated according to the accumulated charge in this potential region.

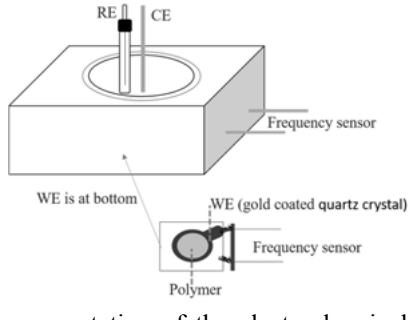

Figure 6. Schematic representation of the electrochemical cell for *in situ* EQCM measurement.

3.2.4 *In situ* electron paramagnetic resonance

In the presence of an external magnetic field B, an unpaired electron can align itself either antiparallel (spin quantum number $m_s = +\frac{1}{2}$) or parallel ($m_s = -\frac{1}{2}$) to the field due to the Zeeman effect. The energy splitting of the two levels is proportional to the magnetic field (*B*) and the electron *g*-factor (*g*). The unpaired electron can move between these states by emitting or absorbing a photon with the energy of *hv*, which equals the energy splitting according to the following equation:

$$E = m_s * g * u_B * B = h * v \quad (6)$$

where u_B is the Bohr magneton.

In practical experiments microwave is used as the photon source with a fixed wavelength while the external magnetic field (*B*) is swept. When the splitting energy of an unpaired electron matches the microwave energy photon absorption occurs and gives rise to a measurable signal, which is proportional to the number of unpaired spins. The *g*-factor can be calculated according to the magnetic field strength (*B*) where photon absorption occurs. The spin concentration can be estimated by the integration of the excitation spectra. *In situ* electron paramagnetic resonance (EPR) is the combination with electrochemical method to monitor the spin signal at different potentials.

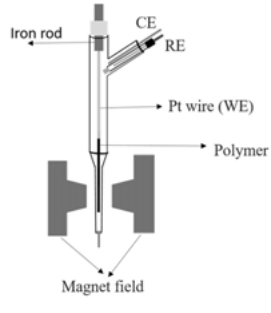

Figure 7. Schematic representation of the electrochemical setup for *in situ* EPR measurement

In this thesis, a Pt wire was used as WE with the lower end of the wire coated with polymer. The cell was positioned with the polymer within the external field while CE and RE were positioned in the top part of the cell (Figure 7). The polymer radical cations produced during doping and semiquinone radicals produced during the pendant redox reaction were investigated to track the backbone doping as well as pendant redox reaction process.

3.2.5 *In situ* conductance

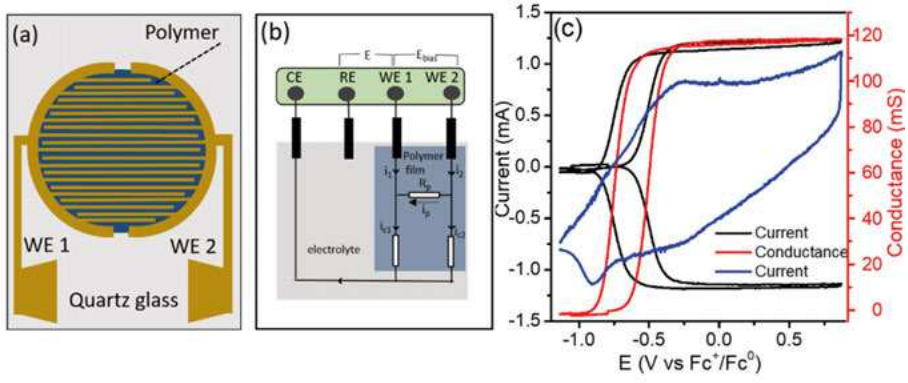

Figure 8. Schematic representation of (a) IDA electrode, (b) three-electrode setup using an IDA as WE. (c) *in situ* conductance measurements from a CV on IDA electrode. The black curve is the current response on the two WEs, the blue curve is the sum of current response on the two WEs and the red curve is the calculated conductance as a function of potential.

Both *in situ* and *ex situ* (*e.g.* four-point probe) technique can be used to measure conductivity. In this thesis, the *in situ* method was used to measure the potential-dependent conductance of conducting polymers, where the conductance results from potential-dependent polymer oxidation (doping)-induced charge-carrier formation. The WE is an interdigitated array (IDA) electrode (Figure 8a), consisting of two WEs. Each WE consists of 90 screen-printed gold fingers with 10 um distance between neighboring electrode pairs (WE1 and WE2). During polymerization the polymer grows on both WEs until the 10 um gap is bridged by the polymer. A potential bias (E_{bias}) is applied between the two WEs. The potential bias used is 1 mV for polymerization and 10 mV for polymer test in this thesis. During CV measurements the current on each electrode is recorded (i_1 and i_2). The sum between these two currents (i_1+i_2) is the current flow to the counter electrode (Figure 8b). The difference between the two currents corresponds to the current flowing through the polymer (i_p) from WE2 to WE1 due to the applied potential bias (*vide infra*). With the potential bias E_{bias} and current flow through the polymer (i_p), the polymer resistance (R_p) as well as the polymer conductance (G_p) can be calculated according to the Ohm´s law:

$$G_p = \frac{1}{R_p} = \frac{i_p}{E_{bias}} \quad (7)$$

where i_p is calculated by the following treatment:

$$i_1 + i_p = i_{c1} \quad (8)$$

$$i_2 - i_p = i_{c2} \quad (9)$$

$$i_p = \frac{(i_2 - i_1) - (i_{c2} - i_{c1})}{2} \quad (10)$$

$\Delta i = i_2 - i_1$, $\Delta i_c = i_{c2} - i_{c1}$, by assuming $\Delta i_c << \Delta i$. This condiation is satisfied throughout the thesis by using sufficicent low CV scan rate.[11] i_p can thus be estimiated directly from the recored current difference Δi from equation (11):

$$G_p = \frac{1}{R_p} = \frac{i_p}{E_{bias}} = \frac{i_2 - i_1}{2E_{bias}} \quad (11)$$

Figure 8c shows the *in situ* conductance measurement of pEDOT. Due to the presence of E_{bias} between WE1 and WE2, equal current magnitudes with opposite sign are observed at the two electrodes. The black curve is the current on each WE (i_1 and i_2) while the red curve is the calculated conductance as a function of applied potential according to equation (11). Below -0.7 V, pEDOT is undoped and thus has low conductance (see section 4.2.2.2). Below -0.7 V the current on the two WEs is low (black curve) and the conductance (red) is neglectable. Above -0.7 V pEDOT is gradually doped, conductance rises and reaches the plateau value at -0.3 V. -0.7 V is known as the doping onset potential while -0.85 V is known as the doping offset potential. In this thesis the potential where the conductance reaches half of the maximum value in the anodic scan (here -0.45 V) is referred to conductance onset potential. The potential where the conductance has decreased to half of the maximum value in the cathodic scan (here -0. 70 V) is referred to conductance offset potential.

4. Organic energy storage materials

LIBs have dominated the market of portable electronics owing to their high energy and power densities. They are also the most promising candidates for energy storage in large-scale power systems such as electric vehicles and smart grids.[12] However, the cathodes in conventional rechargeable lithium-ion batteries are mainly inorganic materials,[13,14] which are expensive and have high CO_2 footprint during the raw material purification and manufacturing process. Organic materials (containing C, H, O, N) are potentially abundant with low energy consumption.[15–19] Replacing the traditional inorganic cathode materials with sustainable organic active materials is expected to decrease the dependence on inorganic energy storage materials.[1–3] In this section, energy storage materials including 1) organic redox molecules, 2) conducting polymers, and 3) CRPs are discussed.

4.1 Organic molecules

Organic redox molecules such as organosulfur,[20–22] radicals[23,24] and carbonyls[25,26] have been widely investigated as energy storage materials. Organosulfur compounds have disulfide bonds (-S-S-), which can undergo a reversible, two-electron transfer reaction through oxidation/reduction (Scheme 1a). They are, in general, low-cost, biodegradable, and relatively nontoxic. However, the organosulfur redox reaction suffers from slow kinetics.[27] Radical compounds, *i.e.* nitroxides and phenoxides, can also be reversibly oxidized (Scheme 1b) at high potentials, thus providing promising high-potential cathode materials. The self-exchange reaction, between the charged state and the radical state, is often fast, thus exhibiting superior reaction kinetics. However, the oxidation of the neutral radical involves only one electron-transfer, giving low capacity.[28] Conjugated carbonyls have significantly higher capacities compared to radical compounds as they can, in many cases, reversibly experience two-electron transfer processes (Scheme 1c). In addition, the structural diversity through substituent provides possibilities to tune the redox potential, making carbonyl compounds extremely popular. Their redox reaction also shows compatibility with various charge-compensating electrolyte cations, such as Li^+,[29] Na^+,[30,31] H^+,[32] Mg^{2+}[33] and Zn^{2+}.[34] Quinone, as one of the simplest carbonyl compound, is particularly attractive. It exhibits a theoretical capacity

of 496 mAh/g and has been widely studied as organic energy storage material. In this thesis, all investigated compounds are based on quinone and its derivatives.

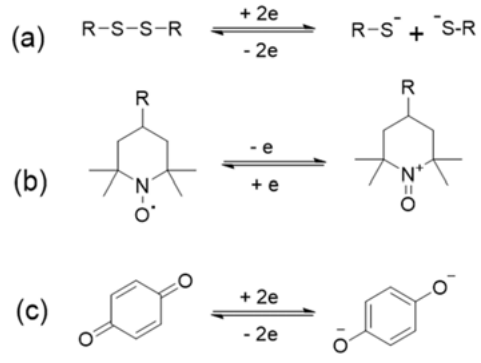

Scheme 1. Redox reaction of (a) organosulfur compounds, (b) organic radical compounds, (c) quinone.

4.2 Conducting polymers

Since the discovery that trans-polyacetylene potentially possesses extremely high electrical conductivity,[35,36] the field of conducting polymers, has attracted the interest of thousands of scientists. The basic difference between a conducting polymer and a traditional, insulating polymer is the free valence electrons. In traditional insulating polymers (*e.g.* polyethylene), the four valence electrons of carbon atom are bound in sp^3 hybridized covalent bonds. Such sigma-bonding electrons are localized and do not contribute to the electrical conductivity of the material. Conducting polymers contain aromatic rings or double bond in the main chains. They are π-conjugated systems with contiguous sp^2 hybridized carbon centers, which bound three of the carbon valence electrons. The last valence electron resides in a p_z orbital, which is orthogonal to the plane of the three sp^2 sigma-bonds. p_z orbitals of the carbon atoms in the conjugated system form wide delocalized π-orbitals. The electrons in the delocalized orbital become mobile when the material is "doped". The conducting mechanism will be discussed in section 4.2.2.2.

Several p-doped conjugated polymers have been used as energy storage materials, including polypyrrole (PPy),[37] polythiophene (PT) ,[38] and polyaniline (PANI).[39–41] Among these conducting polymers, PANI may have benzidine moieties on the polymer backbone, which might yield toxic products upon degradation.[42] PPy is an environmental-friendly system, but it has the disadvantage of low stability.[43–45] PT is stable and has high conductance, and thus has been widely investigated. In this thesis, a thiophene based electron-rich and planar pEDOT[46,47] is used as conducting polymer backbone.

4.2.1 Polymerization

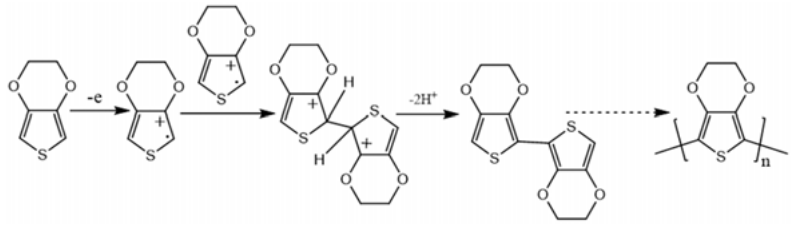

Figure 9. Polymerization mechanism of pEDOT.

Conducting polymers are usually obtained from the chemically or electrochemically driven oxidative polymerization of monomer units. In chemical polymerization, Fe^{3+} or $S_2O_8^{2-}$ are usually used as oxidation agents.[48,49] Chemical oxidation is aggressive and the polymerization process is difficult to control. Electrochemical polymerization include anodic[50] and cathodic polymerization.[51,52] The cathodic polymerization method (*e.g.* polymerization of poly p-phenylene vinylene and polypyridine) is not used frequently due to the harsh condition required. Anodic polymerization is usually used for the polymerization of PANI, PPy, PT and pEDOT.

Polymerization involves several steps: radical formation, dimerization, deprotonation, oligomerization, nucleation, deposition, growth and solid-state process. During the radical formation process, oxidation of the monomer produces a radical cation which can attack and couple to a second radical cation and form a charged dication dimer. The dication then releases two protons and neutral dimer forms (Figure 9). The neutral dimer can be further oxidized and couple to another radical cation unit. The polymer length increases with the continuous polymerization, which is ended by the precipitation of insoluble polymer. In electrochemically driven polymerization the polymer, in favorable cases, precipitates onto the electrode surface. Worth to note is that the conducting nature of the polymer film enables further growth on top of the polymer film when the current collector is covered by a polymer layer. In this thesis, all studied polymers are based on EDOT and are obtained by elecrochemical polymerization.

For electrochemical polymerization, if the polymerization charge and the amount of immobilized repeating units are known, the polymer length can be calculated according to the following equation:

$$x = \frac{2n_t}{2n_t - n_e} \tag{12}$$

where n_e (mol) is the sum of total electron transfer and n_t (mol) is the sum of repeating units. Each polymer contains x repeating units on average and the average chain number is n_t/x. The total number of electrons transferred per

chain is 2*(x-1) and the total number of electrons transferred is n_e=2*(x-1)* n_t/x.

4.2.2 Doping

In conducting polymers each p_z orbital of the carbon atoms in the conjugated system contains one electron. When a p_z orbital couples to another p_z orbital two molecular orbitals form, one antibonding orbital and one bonding orbital. The bonding orbital will be fully occupied by the two electrons (from the two carbon atoms) while the antibonding orbital will be empty. The coupling of all the p_z orbitals in the same conjugated system forms the same number of molecular orbitals whereas half are bonding molecular orbitals and half are antibonding molecular orbitals. The bonding molecular orbitals with closely lying energies make up a band of states called the valance band (VB). The antibonding molecular orbitals, with closely lying energies, make up a band of states called conduction band (CB). The energy difference between the VB and the CB is called the bandgap. The bandgap of a conducting polymer is, typically, around 2 eV.

Some neutral state semiconductors can become conducting through thermal activation of charge carriers according to the Arrhenius equation. However, for conducting polymers, the thermal energy at room temperature is not sufficient to excite electrons from the VB to the CB. To make the polymer conducting at room temperature, a little help is needed to increase the charge carrier concentration. Doping, namely charge transfer to or from the conjugated polymer chains can be introduced to increase the charge carrier concentration through the formation of in-gap states. Reversible charge transfer by doping can be accomplished by chemical doping or electrochemical doping.[39,53,54] According to the charge transfer direction, doping can be classified into p-type doping (polymer is oxidized) and n-type doping (polymer is reduced). A p-doped (n-doped) conducting polymer can be reversibly dedoped to its neutral state though reduction (oxidation).

4.2.2.1 Doping mechanism

In chemical doping, p-type doping signifies electron transfer from the polymer to oxidative dopants, forming positive charges on the conjugated polymer chain. Iodine and bromine are often used as p-type dopants. n-type chemical dopants are usually reductive alkali metals. The dopant concentration affects the charge carrier concentrations as well as the resulting conductance.[55] Chemical doping is an efficient and straightforward process. However, it is difficult to control the doping level and homogeneity.

In electrochemical doping, the doping charge comes from the electrode. The polymer is oxidized at a certain high potential (p-doping) or reduced at a certain low potential (n-doping). Charge-compensating counter ions from the electrolyte compensate the charge on the polymer chain and act as dopants. The charge-compensating counter ions are called dopant. The electrolyte cation is dopant in n-doping and electrolyte anion is dopant in p-doping. The doping level can be controlled by the applied potential on the conducting polymer. In this thesis, electrochemical doping was used to dope the conducting polymers.

In both chemical and electrochemical doping the polymer backbone experience a structure change from aromatic to quinoid-like geometry (Figure10a).[56,57] With the structure change new energy states (bonding in-gap state and antibonding in-gap state) form (Figure 10b).[58,59] The appearance of in-gap states increases the charge carrier density (see section 4.2.2.3).

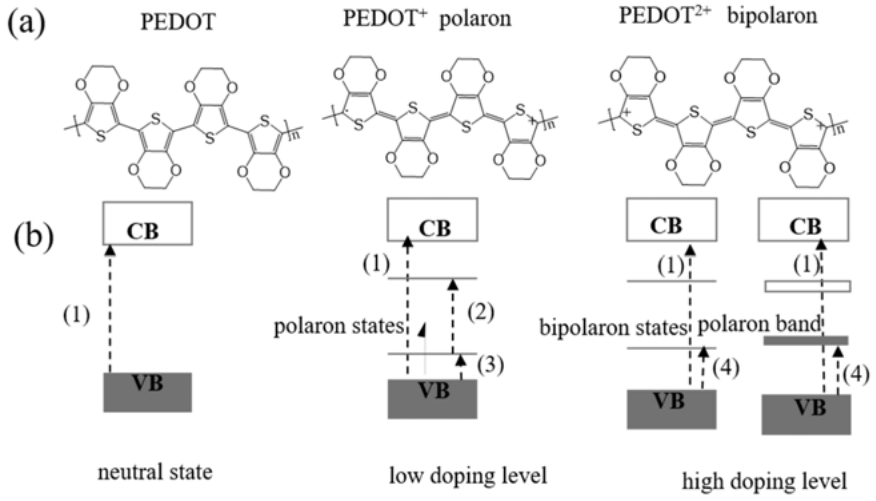

Figure 10. (a) Structure evolution, (b) energy diagrams evolution of pEDOT at different doping levels during p-doping process.

During p-doping electrons from the VB are removed and during n-doping additional electrons are injected into the CB.[60,61] A polymer chain can be reversibly doped by introducing several charges. However, the coulombic repulsion between the consecutively induced charges on the polymer chain determines that the injected charges cannot be introduced at the same potential. The resulting current response of the doping process thus shows a capacitive behavior with a poorly defined doping potential (Figure 11).[62,63] The undefined doping potential suggests that conducting polymer cannot give a fixed charge/discharge plateau in energy storage applications

As the polymer chain becomes positively charged during p-doping. Radical cation (polaron) forms at low doping levels while dication (bipolaron) forms

at high doping level. Both polaron and bipolaron are charge balanced by corresponding counter anions from the electrolyte. The mass change of counter ion uptake (expulsion) upon doping (dedoping) can be monitored by EQCM while the polaron (radical cation) concentration can be monitored by *in situ* EPR.[64]

4.2.2.2 Doping and conductance

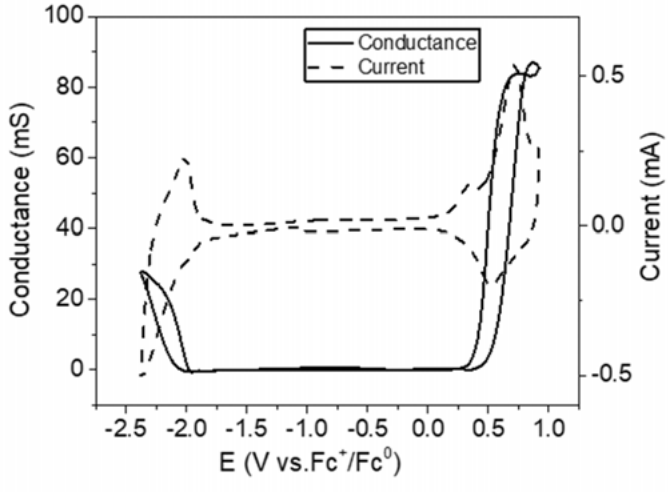

Figure 11. Cyclic voltammograms (dashed line) and *in situ* conductance (solid line) of PT tested in 0.1 M $TBAPF_6$/MeCN

Neutral conducting polymers can undergo oxidative p-doping and become positively charged, forming an in-gap state which is filled by an unpaired electron. The produced radical cation (polaron) is a charge carrier which can be delocalized over a few EDOT monomer units.[65] The radical cation concentration increases with doping level. The unpaired electron in the in-gap state can hop to another in-gap state. From a molecular level, the radical cations can move freely along the same polymer chain or between different polymer chains,[66] thus generating conductance. This explains the tremendous increase of conductance around -0.5 V seen in Figure 8c.

With the increased doping level, the polymer is further oxidized and the unpaired electron in in-gap state is removed, forming spinless dications (bipolaron) (Figure 10b). The formation of bipolaron is the result of thermodynamic competition between polaron and bipolaron.[67] Up to now, polarons are well-documented as charge carrier of conducting polymers. Though subject to debate, based on the conductance response at high doping levels, some research shows that the bipolaron could also contribute to the overall conductance.[68,69]

In this thesis, a decreased polaron concentration at high doping level was indeed observed while the conductance remained relatively constant at high doping level, suggesting that the spinless bipolaron may also contribute significantly to the conductance.

The conductance discussed above is thermally activated hopping for both intra-chain and inter-chain transport. The inter-chain transport has been proved to be the rate-limiting step in most disordered conducting polymer.[70,71] It is worth to note that charge transport in conducting polymers is determined by several factors, *i.e.* chain length, polymer orientation, crystallinity, electrolyte, dopant ion, solvent, and temperature.[72–74] It is well established that both the inter-chain and intra-chain charge transport of conducting polymer can be significantly affected by the structure co-planarity.[75,76] In a highly twisted polymer chain the charge carriers can be localized extensively as a result of decreased π-conjugation, the backbone twisting could result from the bulky side chains as well as its interaction with polymer backbone.[77–80] Hence, the charge transport property is determined by the polymer type as well as by experimental conditions.

PT and its derivatives show both p-doping and n-doping capability. In general, n-type conducting polymers are not as stable as p-type polymers. The reduction of a conducting polymer usually occurs at a rather negative potential and the reduced state is vulnerable to oxygen and moisture in the air. In addition, the conductance and reversible charge of p-doping is, in general, higher than those of n-doping (Figure 11). Up to now, one reported stable n-doped conducting polymer is poly (phenylthiophene) where the electron-deficient phenyl group can delocalize and stabilize the radical anion[70].

4.2.2.3 Doping and bandgap evolution

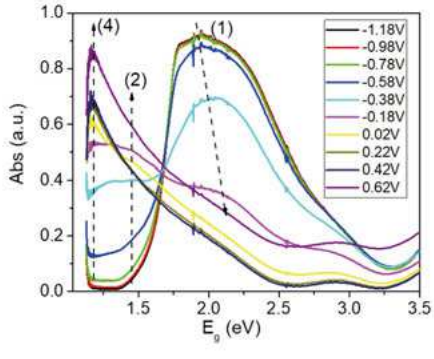

Figure 12. *In situ* UV-vis spectroscopy of PEDOT on ITO at different potentials. (1), (2) and (4) represent the transition 1, 2 and 4 in Figure 10b, respectively.

Changes in doping-induced energy states can be monitored by *in situ* UV-vis spectroscopy (Figure 12). At neutral state, the CB-VB bandgap transition of conducting polymers gives the maximum absorbance at around 2.0 eV in the visible region. This energy gap of conducting polymers is affected by the conjugation length and is widely discussed in electrochromic devices.[81,82] During p-doping electrons from the VB are removed, causing depletion of the VB as well as the formation of in-gap states. As a result, the absorption peak corresponding to the CB-VB transition at 2.0 eV decreases (transition 1 in Figure 10b) and blue shifts.

The depletion of VB upon p-doping is also accompanied by the appearance of new absorption peaks at 1.4 eV corresponding to transitions involving bonding and antibonding in-gap states (transition 2 in Figure 10b)[83,84] in the visible region and VB/bonding in-gap states (transition 3) in the IR light region. Further doping produces more in-gap states which are empty as the unpaired electron is taken away. These in-gap states overlap and form the bipolaron band. With the depletion of the VB and formation of the bipoalron band the VB-bipoalron band transition (transition 4) blue shifts to visible region at 1.2 eV and the absorbance keeps increasing with the doping level.

4.3 Conducting redox polymers

As discussed above the doping of conducting polymers is reversible, enabling the storage and release of charge. This characteristic makes conducting polymers a viable alternative as energy storage materials. However, limited by the low doping level where each EDOT unit can store one charge at most, the capacity of conducting polymers is rather low. Though high doping levels can increase the charge storage capacity, it also leads to irreversible degradation of the conducting polymer in a process known as over-oxidation. Moreover, since the doping is potential-dependent, conducting polymers cannot provide a fixed operating potential required for battery electrode materials. Rather, conducting polymers display sloping charging/discharging curves (capacitive behavior) and thus are often used as capacitors instead of batteries.

Small organic molecules have high capacity and well-defined redox potential. However, they often suffer from dissolution and low electronic conductivity as energy storage materials. The conducting property and polymeric structure of conducting polymers enable application as a conducting and polymeric agent to provide conductance for insulating capacity-carrying organic molecules as well as to prevent dissolution of the organic molecules. We have synthesized a series of CRPs, where redox-active quinones are functionalized onto polymerizable monomeric or trimeric units.[85–94] The conducting polymer structure, based on pEDOT, is conducting and thus removes the conductive additives.

A fundamental requirement to make a CRP is redox matching, *i.e.* the redox potential of capacity-carrying quinone must be within the conducting region (potential window) of the polymer backbone.[95] The conducting region of pEDOT is relatively stable with respect to electrolyte while the redox potential of quinone is highly dependent on the cycling electrolyte. This thesis starts with the discussion on the quinone redox chemistry to explore the possible redox matching with pEDOT backbone with the final aim to design high performance CRPs as energy storage materials.

5. Quinone based CRPs and battery evaluation

5.1 The Quinone redox chemistry

As discussed above, the principle design criteria for fabricating a CRP is that redox matching between the quinone redox potential and the conducting region of conducting polymers is achieved. Besides, a linker that ensures that the functions of the two individual components are preserved in the CRP, is also necessary. The conductance of pEDOT based polymer usually initiates from -0.7 V and can be reversibly doped up to 0.8 V, giving a -0.7 V_0.8 V conducting window. Thus, quinone redox reactions occurring in this potential region are expected to be redox matched with the pEDOT backbone. The conducting region of conducting polymer is relatively stable with respect to the nature of solvent and counter ions in the electrolyte. However, the quinone redox potential can be affected by various factors, *e.g.* charge-compensating counter ions,[96,97] solvent,[98] and substituents.[26] The first step in this thesis is to investigate how the quinone redox potential is affected by these internal and external factors.

5.1.1 Effect of electrolyte cation and solvent on the quinone redox potential

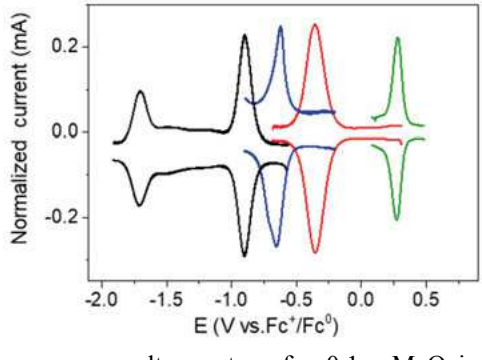

Figure 13. Square wave voltammetry of a 0.1 mM Q in 0.1 M $TBAPF_6$/MeCN (black), 0.1 M $LiClO_4$/MeCN (blue), 0.5 M H_2SO_4/H_2O (green) and a 5 mM quinone

solution in 0.1 M pyridium triflate/0.1 M pyridine/MeCN (red). All measurements were conducted using a bare GC working electrode at the frequency of 8 Hz.

The electrochemical properties of various quinone were characterized in four different electrolytes to study the counter ion and solvent effect on the quinone redox properties (Figure 13), (**Paper I)**. In tetrabutylammonium hexafluorophosphate/acetonitrile ($TBAPF_6$/MeCN), SWV shows two largely separated redox peaks centered at -0.91 V and -1.71 V. The two peaks are attributed to the redox conversion of quinone/semiquinone radical anion (Q/Q^{-}) and semiquinone radical anion/reduced quinone dianion (Q^{-}/Q^{2-}), respectively (Scheme 2a). During the two reduction processes, no counter ion is introduced to balance the negative charge on the Q^{-} or Q^{2-}, as the bulky TBA^{+} has no access to the charged center on quinone. DFT calculation shows that the injected electron during the first reduction step is uniformly delocalized within the molecule, with each oxygen atom accommodating 17.5 % of the injected negative charge. The second reduction step therefor requires a higher driving force to inject the second electron compared to the first reduction step. The interaction terms were used to quantify the coulombic repulsion between the two successive injected charges, which were calculated by multiplying the charge-change at each atom in the first and the second reduction process and creating a sum of interaction terms for the entire molecule. The interaction term is 0.11 for TBA^{+}-cycling.

In $LiClO_4$/MeCN electrolyte, a broad reduction peak with two overlapping peaks centered at -0.63 V and -0.70 V were observed. The two peaks were attributed to the $Q/LiQ^{\cdot}$ and $LiQ^{\cdot}/Li_2Q$ redox conversion, respectively. When switching from TBA^{+} to Li^{+}-cycling, both redox peaks shifted positively. This effect was attributed to the Li^{+} stabilization effect due to Li-O bond as depicted in Scheme 2b. During the first electron-injection process, the Li^{+} ion uptakes 26 % of the injected charge, leaving only 74 % of the injected electron charge in the aromatic system. 74 % is much smaller compared to the 100 % in TBA^{+} electrolyte. This charge-balancing effect of counter ion significantly decreases the electron density on the seimiquinone aromatic ring, making the second electron-injection process easier. During the second electron-injection process, the second counter-balanced Li^{+} uptakes 35 % of the injected electron charge and the first counter-balanced Li^{+} takes further 11 %, thus stabilizing the reduced state significantly. The coulombic interaction term is only 0.07 for Li^{+}-cycling, indicating a significantly decreased coulombic repulsion between the two injected charges, which explains the smaller separation between the first and second reduction peaks in the Li^{+} case compared to that in TBA^{+}-cycling.

In protic pyridium triflate/pyridine/MeCN electrolyte (pKa=5.2), only one pair of redox peaks, centered at -0.35 V, corresponding to $2e/2H^{+}$ transfer of Q/QH_2 redox conversion was observed, indicating that the semiquinone radi-

cal state (QH^-), depicted in Scheme 2c, is unstable with respect to disproportionation. The formal potential shifted positively compared with Li^+-cycling, suggesting further increased counter ion stabilization effect through the H-O bond. During the first electron-injection process, the charge-balancing H^+ uptakes 67 % of the injected charge, leaving only 33 % on the aromatic system. During the second electron-injection process, the second counter-balanced H^+ uptakes 69 % of the injected charge and the first charge-balanced H^+ further takes 2 % of the injected charge. The charge balancing proton thus accommodates most of the injected negative charge, leaving the semiquinone with lower electron density compared to semiquinone with Li^+ and TBA^+-cycling. The coulombic interaction decreased to 0.01 with proton cycling, explaining the disproportionation of the semiquinone intermediate.

In 0.5 M H_2SO_4/H_2O electrolyte (pH=0.3), only one pair of redox peaks centered at 0.27 V corresponding to Q/QH_2 redox conversion was observed. The formal potential further shifted positively compared with H^+-cycling in MeCN electrolyte.

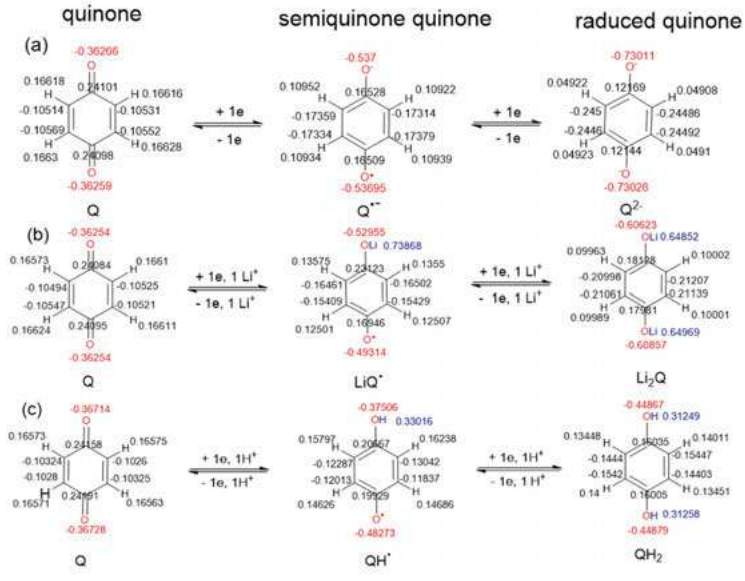

Scheme 2. Quinone redox reactions in (a) $TBAPF_6$/MeCN, (b) $LiClO_4$/MeCN (c) MeCN or H_2O containing H^+ solution. The numbers are the calculated Mulliken charge on each atom.

5.1.2 Substituents effect on quinone redox potential

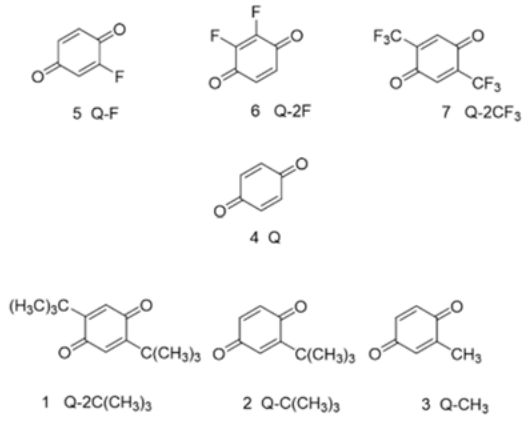

Scheme 3. Structure of the quinone derivatives.

Table 1. Experimental formal potentials of quinone derivatives in four different electrolytes. H^+/MeCN represents 0.1 M pyridium triflate/0.1 M pyridine/MeCN

E^0 (V vs. Fc^+/Fc^0)	**In TBA^+/MeCN**			**In Li^+/MeCN**			**In H^+/MeCN**	**In H^+/H_2O**
	$Q/Q^{\cdot-}$	$Q^{\cdot-}/Q^{2-}$	ΔE	$Q/LiQ^{\cdot}$	$LiQ^{\cdot}/Li_2Q$	ΔE	Q/QH_2	Q/QH_2
$Q\text{-}2C(CH_3)_3$	-1.10	-1.88	0.78	-0.83	-0.83	0	-0.67	insoluble
$Q\text{-}C(CH_3)_3$	-1.00	-1.79	0.79	-0.74	-0.74	0	-0.48	0.16
$Q\text{-}CH_3$	-0.98	-1.78	0.80	-0.71	-0.71	0	-0.40	0.22
Q	-0.90	-1.71	0.81	-0.63	-0.70	0.07	-0.35	0.27
Q-F	-0.77	-1.71	0.86	-0.53	-0.60	0.07	-0.33	0.27
Q-2F	-0.65	-1.53	0.88	-0.48	-0.56	0.08	-0.26	0.27
$Q\text{-}2CF_3$	-0.37	-1.31	0.94	-0.28	-0.52	0.24	-0.20	0.28

Apart from the charge-compensating cation effects discussed above, the formal potential of quinone can also be tailored by the introduction of substituent. This is explained by the increased or decreased electron density on the quinone aromatic system induced by the electron-donating or electron-withdrawing substituent. To systematically investigate the substituent effect on the quinone formal potential, a series of quinone derivatives (Scheme 3) with both electron-donating and electron-withdrawing groups were synthesized and characterized in the four electrolytes above (**Paper I)**. The formal potentials are summarized in Table 1. In $TBAPF_6$/MeCN electrolyte, the formal potential of both $Q/Q^{\cdot-}$ and $Q^{\cdot-}/Q^{2-}$ redox conversion shifted positively with electron-withdrawing ability of the substituent. In addition, the separation between the two redox peaks increased from 0.78 V with $-2C(CH_3)_3$ substitution to 0.94 V with $-2CF_3$

substitution. This indicates that the coulombic repulsion between the two successively injected charges increases with the electron-withdrawing power of the substituent, which was confirmed by the increased coulombic interaction term with electron-withdrawing substituents (Figure 14a). With Li^+-cycling the redox peaks also shifted positively with the electron-withdrawing ability of the substituent. The $2e/2Li^+$ redox conversion observed for quinones with electron-donating substituents turned into two separate $1e/1Li^+$ redox conversions for quinones with electron-withdrawing substituents. This is in accordance with the increase of coulombic interaction term with the electron-withdrawing ability of the substituent (Figure 14a). With H^+-cycling in MeCN, all quinone derivatives show $2e/2H^+$ redox conversion and the formal potential also shifted positively with the electron-withdrawing ability of substituents (Table 1).

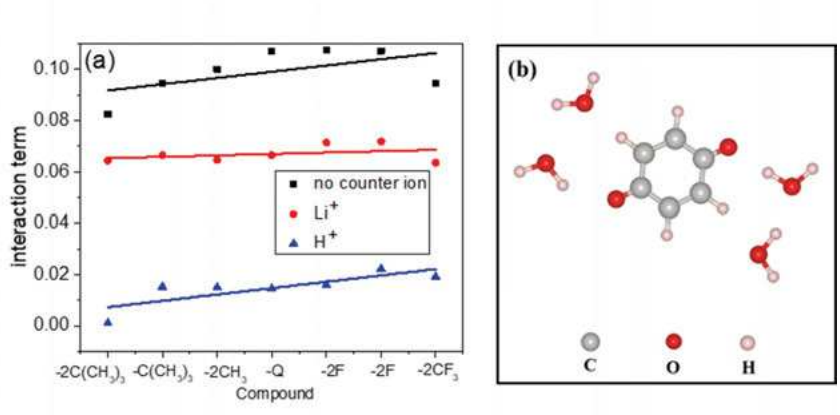

Figure 14. (a) Interaction terms for substituted quinones with TBA^+ (black), Li^+ (red) and H^+-cycling (blue) counter ions. The substituents are ranked according to their electron-withdrawing power. (Solid lines are guides for the eye.) (b) Structure of quinone in a neutral state in an explicit implicit solvent model with four explicit water molecules introduced.

In H_2SO_4/H_2O aqueous electrolyte all quinone derivatives show a pair of redox peak corresponding to $2e/2H^+$ redox conversion. However, the dependence of formal potential on substituent is only seen for electron-donating substitutions. With electron-withdrawing substitutions the effect of substituent was largely lost. Since the only difference between the two H^+-cycling case is the solvent, we attribute this break-down of formal potential dependence on electron-withdrawing substituent to specific solvent-quinone interactions. To investigate the specific quinone-water interaction, DFT calculations with explicit treatment of the water solvent were conducted. The Mulliken charges on the quinone and the introduced four water molecules were calculated. The calculation shows that the water molecules close to carbonyl groups donate elec-

tron density to the quinone (Figure 14b), thus counteracting the electron-withdrawing effect of substituent and causing the break-down the dependence of formal potential on electron-withdrawing substituent.

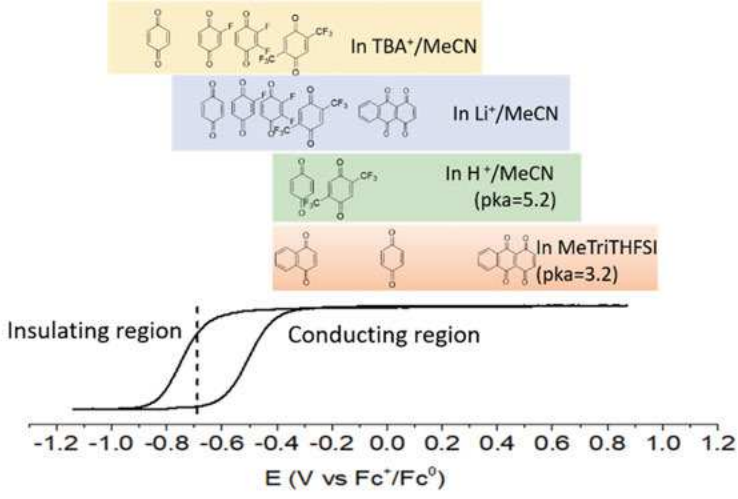

Figure 15. Potential matching of pEDOT conducting region (bottom panel) and the formal potential of quinone derivatives upon TBA^+-(yellow), Li^+-(blue), proton (pKa=5.2, green) and proton (pKa=3.2, orange) cycling.

From these results an initial assessment of the redox matching between substituted quinones and PEDOT could be made. In $TBAPF_6$/MeCN, despite the up-shift of the formal potential caused by the substituent, only the $Q/Q^{\cdot-}$ redox conversion of -2F and $-2CF_3$-substituted quinone derivatives are redox matched with pEDOT (yellow bar in Figure 15). In $LiClO_4$/MeCN, both $Q/LiQ^{\cdot}$ and $LiQ^{\cdot}/Li_2Q$ redox conversions of quinones with electron-withdrawing substitutions are expected to be redox matched with pEDOT (blue bar in Figure 15). With proton cycling in MeCN (pKa=5.2), most quinone derivatives are expected to be redox matched with the pEDOT backbone.

5.2 Quinone based CRPs for Li^+-cycling

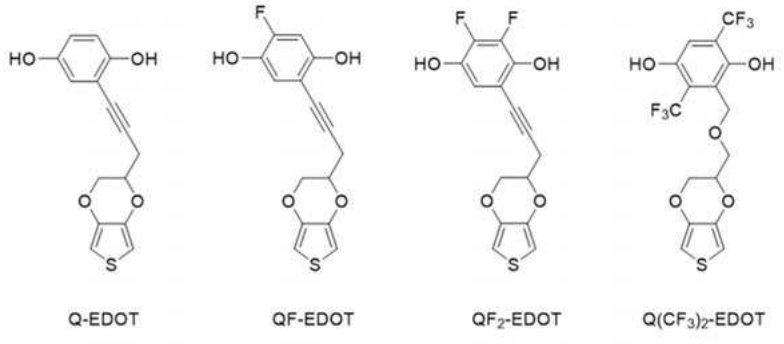

Scheme 4. Structure of the quinone-EDOT based monomer

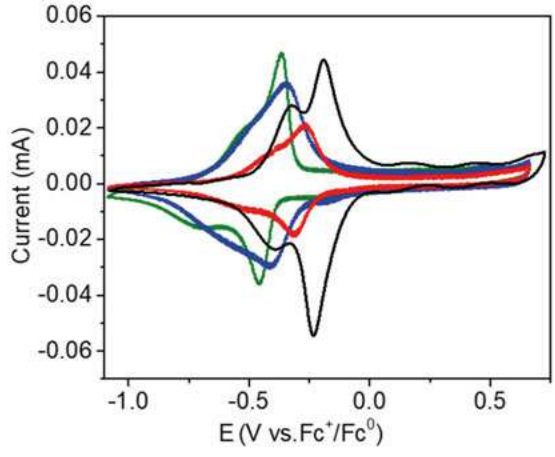

Figure 16. Cyclic voltammograms of Q-pEDOT (green), QF-pEDOT (blue), QF_2-pEDOT (red), $Q(CF_3)_2$-pEDOT (black) on a GC electrode in 0.1 M $LiClO_4$/MeCN at a scan rate of 0.1 V/s.

As discussed above, the formal potential of quinones upon Li^+-cycling can be tuned positively by 0.35 V by electron-withdrawing substituents. The positively shifted quinone formal potentials are expected to be within the conducting region of the pEDOT backbone. To study the expected redox matching between pEDOT and quinone derivatives upon Li^+-cycling, quinone derivatives were functionalized onto EDOT units through a non-aromatic linker (**Paper II)**. Q-EDOT, QF-EDOT, QF_2-EDOT and $Q(CF_3)_2$-EDOT (Scheme 4) monomers were synthesized and electrochemically polymerized from the monomer solution using $TBAPF_6$/MeCN as electrolyte. Deprotonation/lithiation of the obtained polymer was achieved by dipping the polymer in 1 M

lithium tert-butoxide/THF solution. The deprotonated CRPs were characterized by CV in 0.1 M $LiClO_4$/MeCN. All four CRPs shows two pairs of quasi-reversible redox peaks (Figure 16), which are attributed to the Q/$LiQ^{\cdot}$ and the $LiQ^{\cdot}$/Li_2Q redox conversions, respectively. The redox peak of $LiQ^{\cdot}$/Li_2Q is broader compared to that of Q/$LiQ^{\cdot}$. The seemingly capacitive current underlying the redox peaks is attributed to reversible doping/dedoping of the pEDOT backbone. With the electron-withdrawing substituents, the formal potentials of Q/$LiQ^{\cdot}$ and $LiQ^{\cdot}$/Li_2Q redox conversion shifted positively compared to unsubstituted quinone, as expected.

5.2.1 Conductance delay

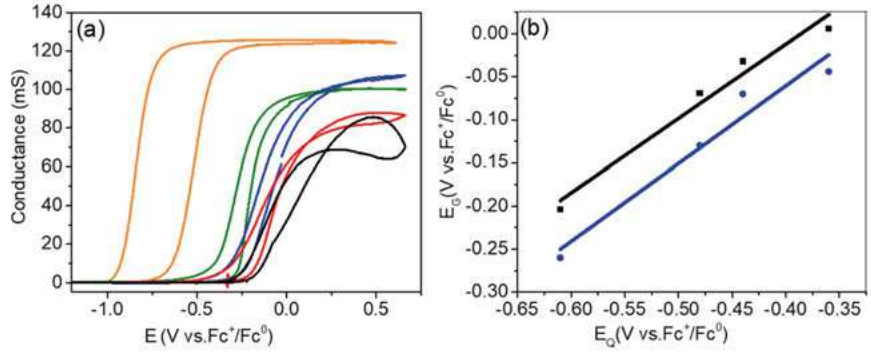

Figure 17. *In situ* conductance of pEDOT (orange), Q-pEDOT (green), QF- pEDOT (blue), QF_2- pEDOT (red), and $Q(CF_3)_2$- pEDOT (black) on IDA-Au electrodes in 0.1 M $LiClO_4$/MeCN at 0.05 V/s, the potential bias between the two working electrodes is 10 mV. (b) Correlation between the backbone conductance onset (black), offset potential (blue) E_G and the $LiQ^{\cdot}$/Li_2Q redox potential E_Q.

In situ conductance measurements were conducted to monitor the conductance of the four CRPs as well as its evolution with potential (**Paper II**). Figure 17a shows the *in situ* conductance of the CRPs together with the corresponding data for pEDOT. The potential where the conductance initiates (above -0.3 V) for the CRPs occurs at much higher potentials than that for pEDOT (-0.7 V). Zotti reported a threshold-doping for polymer conductance, which is attributed to charge carrier localization as a result of backbone twisting caused by bulky side chains.[77,78] Herein, the higher doping threshold was initially attributed to the steric hindrance caused by the bulky pendant quinone. However, a close inspection shows that the potential where the conductance initiates in the four CRPs are surprisingly different despite the four CRPs have quinone pendants of similar size. The conductance onset potential (black) and the conductance offset potential (blue) shows a clear correlation with the for-

mal potential of the quinone second reduction ($LiQ^{\cdot}/Li_2Q$) (Figure 17b), indicating that the lithiated reduced state of the quinone plays a significant role in hindering the conductance of pEDOT backbone. The lithiated, reduced state of quinone may pin the positively charged charge carrier polarons, causing the localization of charge carriers.

5.2.2 Doping onset *vs* conductance onset

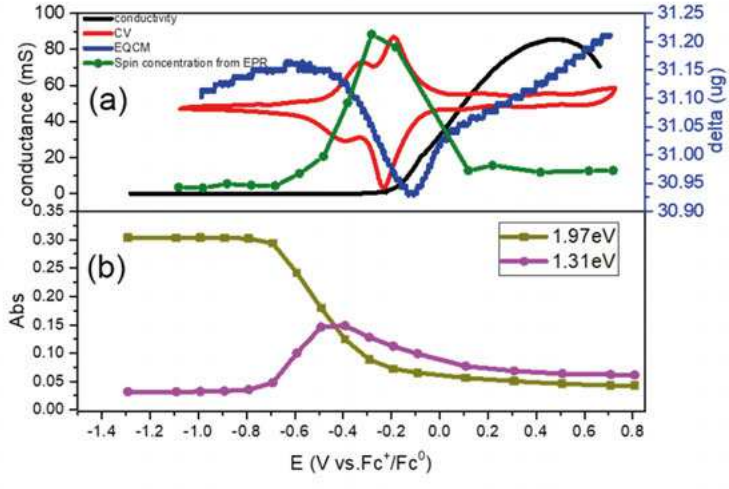

Figure 18. Characterization of $Q(CF_3)_2$-pEDOT in 0.1 M $LiClO_4$/MeCN. Panel (a) shows 1) the tenth sweep CV response of $Q(CF_3)_2$-EDOT on GC electrode at 0.1 V/s (red). 2) *in-situ* conductance during an anodic CV sweep at 0.05 V/s using on IDA-Au electrode (black). 3) the mass change during anodic CV scan on EQCM-Au electrode at 0.1 V/s (blue). 4) the spin concentration as function of potential of a $Q(CF_3)_2$-layer on a platinum wire (green). Panel (b) shows the UV-vis absorbance of $Q(CF_3)_2$-pEDOT measured *in situ* during electrochemical redox conversion of the polymer layer coated on ITO as function of potential at energies of 1.97 eV (brown) and 1.31 eV (pink).

To investigate the origin of the conductance delay, a study of the backbone doping process was undertaken (**Paper II**). *In situ* EQCM, *in situ* UV-vis and *in situ* EPR were used to study the doping process of the four CRPs. *In situ* EQCM shows that the polymer mass started to increase at -0.8 V (blue curve in Figure 18a). This mass increase is attributed to the doping-induced ClO_4^- anion uptake to balance the positive charge of polymer chain, suggesting that backbone is doped already at -0.8 V. The onset doping potential of CRP is similar as that of unsubstituted pEDOT.[99] Between -0.5 V and -0.15 V an extensive mass decrease was observed. It is attributed to the Li^+ expulsion as the reduced Li_2Q-state undergoes the $Li_2Q/LiO^{\cdot}$ and $LiO^{\cdot}/Q$ redox conversions.

Above -0.15 V the polymer mass again increased due to the polymer backbone doping-induced ClO_4^- uptake. *In situ* UV-vis spectroscopy shows that the absorbance at 1.97 eV, corresponding to the CB-VB transition (transition 1 in Figure 10b), decreased initially from -0.7 V (brown curve in Figure 18b). This is attributed to the depletion of electrons from the VB as the polymer is oxidized. The absorbance at 1.31 eV, corresponding to the bonding/antibonding in-gap state transition (transition 2 in Figure 10b), increased initially from -0.7 V (pink curve in Figure 18b), indicating the formation of polarons.

The *in situ* EPR curve closely matches the peak in cyclic voltammograms. To be specific, *in situ* EPR monitored a rather low spin concentration below -0.7 V, which then increased over the $Li_2Q/LiO^{\cdot}$ redox conversion and reached the maximum value at -0.3 V (green curve in Figure 18a). After that the spin concentration decreased over the $LiO^{\cdot}/Q$ redox conversions. At even higher potentials above 0.1 V, the spin concentration kept a constant value with further doping.

The *g*-value is often used to identify the nature of the unpaired electron as *g*-value represents the magnetic environment of the radical.[100] It is worth to note that the *g*-value below -0.6 V is similar as that above 0 V while the *g*-value between -0.6 V and -0.2 V is significantly higher (Figure 19b). This suggests that the polaron is the dominant spin species below -0.6 V and while above 0 V the $LiO^{\cdot}$ radical is the dominant spin species over the $Li_2Q/ LiQ^{\cdot}$ redox conversion peak. Importantly, the increase in spins concentration between -0.7 V and -0.6 V is originating from polaron formation induced by doping of the polymer backbone, rather than from the $LiO^{\cdot}$ radical. The minor residual spin existing below -0.7 V is thus attributed to the backbone polaron. From *in situ* EQCM, *in situ* UV-vis and *in situ* EPR methods, it is thus concluded that the pEDOT backbone doping initiated at -0.7 V. However, the conductance initiated much later, indicating that the doping-produced charge carriers were localized and mostly immobile to some extent before the Li_2Q state quinone was oxidized.

5.2.3 Nature of the Radicals

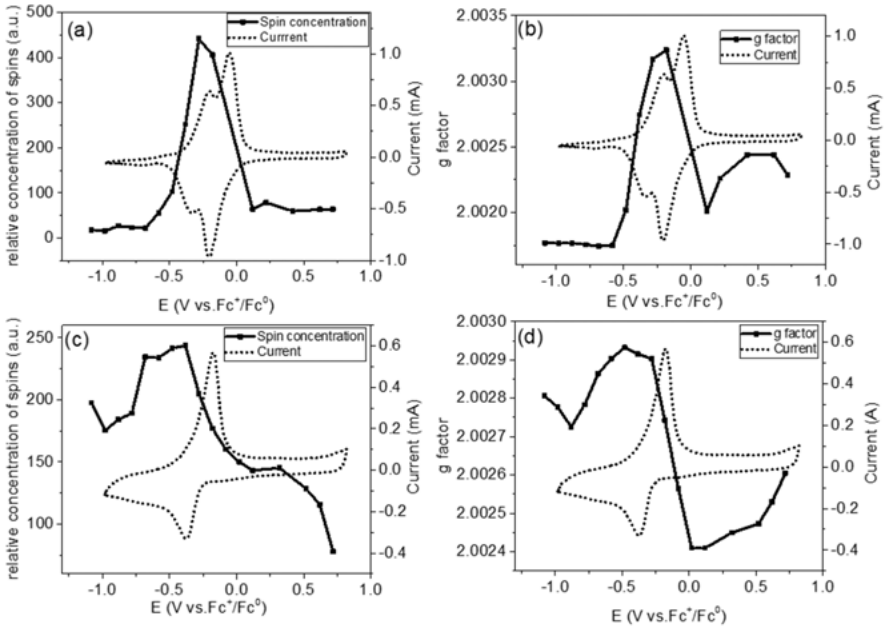

Figure 19. Concentrations of spins of (a) $Q(CF_3)_2$-pEDOT and (c) Q-pEDOT as function of potential, the corresponding *g*-value for the observed spins in (b) $Q(CF_3)_2$-pEDOT and (d) Q-pEDOT. Dotted lines show the CV response of the corresponding electrodes measured prior to the EPR experiment in a beaker cell in 0.1 M $LiClO_4$/MeCN at 0.1V/s.

The substitution of $–CF_3$ on the quinone aromatic ring cannot only tune the formal potential to give a high potential quinone based LIB cathode, but also improve other aspects of the electrochemical response. Figure 19c shows that Q-pEDOT had a relatively high spin concentration below -0.7 V which then increased over the $Li_2Q/LiQ^{\cdot}$ anodic peak and reached the maximum at -0.3 V. Subsequently, the spin concentration decreased dramatically upon the $LiO^{\cdot}/Q$ oxidation and reached a relatively constant value at -0.1 V. Above 0.3 V, further doping caused the removal of unpaired electrons in in-gap states and thus a decrease of spin concentration. Unlike the polaron being the dominant spin species below -0.6 V in $Q(CF_3)_2$-pEDOT. The *g*-value of Q-pEDOT is constant between -1 V and -0.4 V (Figure 19d). Above -0.4 V, the spin concentration decreased with the consumption of $LiQ^{\cdot}$ from the $LiQ^{\cdot}/Q$ redox conversion. This suggests that the $LiQ^{\cdot}$ radical, rather than the backbone polaron, is the dominant spin species between -1 V and -0.4 V. The residual spin concentration (below -0.7 V) is thus assigned to the trapped $LiQ^{\cdot}$ radicals rather than polymer backbone polarons. The trapping of $LiQ^{\cdot}$ radicals results from the loss of conductance. To be specific, in the cathodic scan the pEDOT

backbone becomes insulating before $LiQ^{\cdot}$ is fully reduced to Li_2Q. It is thus concluded that the $–CF_3$ substituent can increase the quinone formal potential, thereby avoiding the trapping of $LiQ^{\cdot}$ radicals and improving the conversion efficiency of $Li_2Q/LiQ^{\cdot}$. This makes $Q(CF_3)_2$-pEDOT a promising CRP based LIB cathode candidate with high voltage output as well as high practical capacity.

5.2.4 LIBs with Quinone based cathode

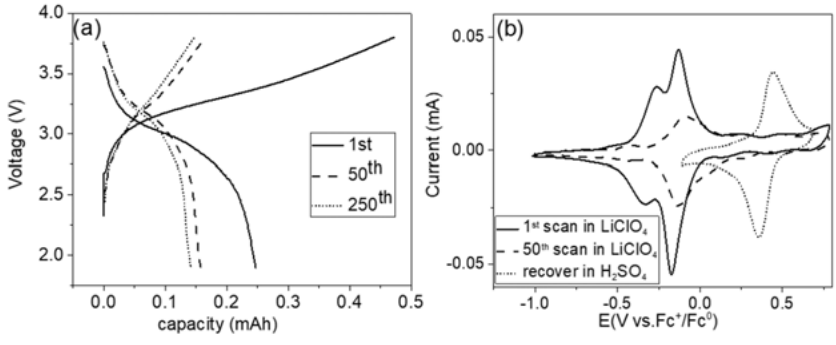

Figure 20. (a) $Q(CF_3)_2$-pEDOT battery performance: galvanostatic charge discharge curves of the 1st (solid line), 50th (dashed line) and 250th (dotted line) cycles in 0.2 M $LiPF_6$/PC. (b) Cyclic voltammograms of $Q(CF_3)_2$- pEDOT electrode: 1st scan (solid line) and 50th scan (dashed line) in 0.1 M $LiClO_4$/MeCN at 0.1 V/s, 1st scan (dotted line) after the same electrode was transferred to 0.5 M H_2SO_4/H_2O.

Due to the promising properties of $Q(CF_3)_2$-pEDOT, a $Q(CF_3)_2$-pEDOT cathode was used in a battery with Li metal as anode and 0.2 M $LiPF_6$/PC as electrolyte **(Paper II)**. Figure 20a shows that this battery gave two successive discharge plateaus centered at around 2.9 V and 3.2 V, indicating that the $Q(CF_3)_2$-pEDOT can indeed be used as cathode material for LIBs. However, only 67 % of the initial discharge capacity was retained after 250 cycles. A CV stability test in a three-electrode setup shows that the charge of second reduction ($LiQ^{\cdot}/Li_2Q$) disappeared after 50 scans, presumably due to the loss of redox matching upon prolonged cycling. Surprisingly, 20 % of the charge recovered when the cycled electrode was transferred to, and cycled in a 0.5 M H_2SO_4/H_2O electrolyte, where the Q/QH_2 redox reaction occurs at 0.38 V and is in perfect redox matching with the pEDOT conducting region. This finding indicates that thick $Q(CF_3)_2$-pEDOT films suffer from redox mismatching, presumably due to the limited electron transport in thick polymer film at low doping levels. To make a stable CRP based LIB cathode, the redox matching

must be improved. This could be achieved by increasing the pendant group redox potential even further.

5.3 Quinizarin cathode based LIB battery

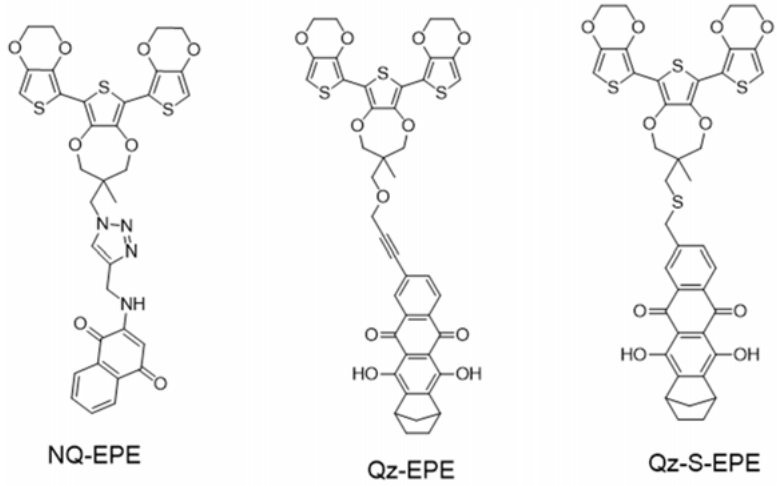

Scheme 5. Structure of the quinone derivatives functionalized onto EPE trimer

Based on the study above it is clear that the redox matching between the quinone redox potential and the backbone conducting region must be improved to make a stable LIB cathode. Figure 15 shows the redox potential of some quinone derivatives with different cycling ions together with the potential-dependent conductance for pEDOT. The formal potential of quinizarin (Qz) upon Li^+-cycling is well within the pEDOT conducting region. Therefore, the high potential Qz was functionalized onto a EDOT-3,4-propylenedioxythiophene (ProDOT)-EDOT (EPE). The resulting Qz-S-EPE was electrochemically polymerized to form poly (Qz-S-EPE) where Qz is used as capacity-carrying pendant group (Scheme 5) **(Paper III)**.

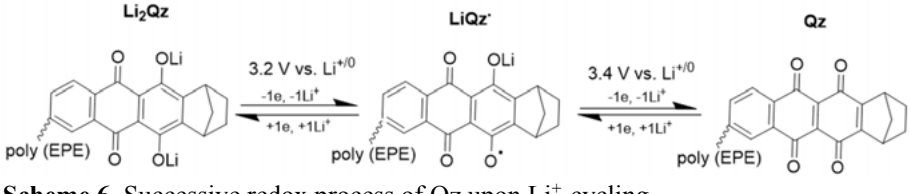

Scheme 6. Successive redox process of Qz upon Li^+-cycling.

5.3.1 Redox match

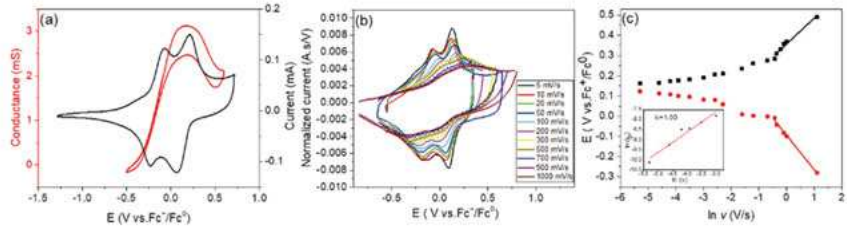

Figure 21. Poly (Qz-S-EPE) (a) *In situ* conductance on IDA-Au (red) and cyclic voltammograms (black) on GC in 0.1 M $LiClO_4$/MeCN, (b) Cyclic voltammograms with normalized current on GC at scan rates of 5-1000 mV/s in 0.1 M $LiClO_4$/MeCN, (c) scan rate dependence of corresponding peak potential of $LiQz^{\cdot}$/Qz redox conversion. The inset shows the correlation of ln (i_p) ~ln (v) curve for the anodic scan.

The cyclic voltammograms of Poly (Qz-S-EPE) shows two pairs of redox peaks centered at -0.2 V and 0.1 V, which are attributed to the $Li_2Qz/LiQz^{\cdot}$ and $LiQz^{\cdot}$/Qz redox conversions (Scheme 6), respectively. The polymer conductance initiated from -0.4 V and reached the maximum value at around 0.1 V (Figure 21a). The formal potentials for both the $Li_2Qz/LiQz^{\cdot}$ and the $LiQz^{\cdot}$/Qz redox conversion are located within the polymer conducting region. The conductance at the $Li_2Qz/LiQz^{\cdot}$ redox potential is half-way to the maximum conductance value while the conductance at the $LiQz^{\cdot}$/Qz redox potential is at the maximum value. The polymer conductance is thus sufficiently high to provide efficient electron-transport pathways for Qz redox conversion. Kinetic studies show that the peak potential did not change with scan rate when the scan rate is less than 50 mV/s (Figure 21b). The peak current of both $Li_2Qz/LiQz^{\cdot}$ and $LiQz^{\cdot}$/Qz redox conversions increased linearly with scan rate, indicating that $Li_2Qz/LiQz^{\cdot}$ and $LiQz^{\cdot}$/Qz redox conversions are thermodynamically controlled. At scan rates above 50 mV/s, however, the peak separations increased with the scan rate, indicating that $LiQz^{\cdot}$/Qz redox conversion are kinetically controlled at higher scan rates. The rate constants for the $LiQz^{\cdot}$/Qz and $Li_2Qz/LiQz^{\cdot}$ redox conversions were estimated to be 1.5 s^{-1} and 0.7 s^{-1}, respectively, suggesting redox conversion rates on the time-scale of seconds.

5.3.2 Battery performance evaluation

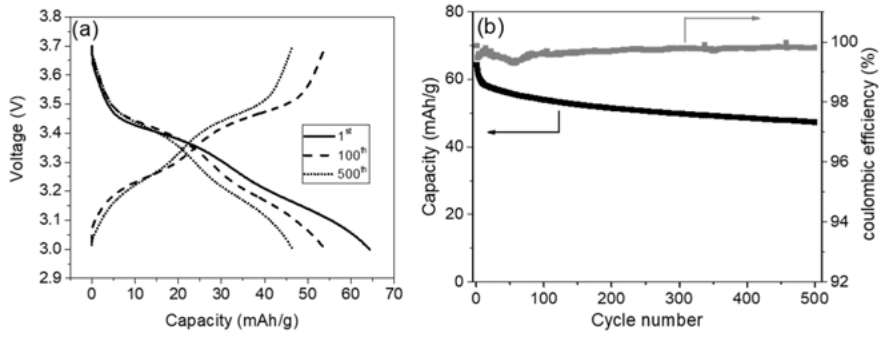

Figure 22. Poly (Qz-S-EPE) LIB battery evaluation: (a) galvanostatic charge−discharge profiles at 1.5 C in 1 M $LiPF_6$/EC/DEC electrolyte, (b) Galvanostatic discharge capacities (black) and coulombic efficiency (grey) at a rate of 1.5 C for the 500 cycles.

The prepared poly (Qz-S-EPE) was assembled into a LIB with a Li metal as anode **(Paper III)**. Figure 22a shows the galvanostatic charge-discharge profiles of the battery. Two discharge plateaus, centered at 3.2 V and 3.4 V, were observed. In accordance with the results from three-electrode setup, the two plateaus are attributed to the $Li_2Qz/LiQz^-$ and the $LiQz^-/Qz$ redox conversions, respectively. As expected, this voltage output is somewhat higher than that of the $Q(CF_3)_2$-pEDOT based battery (3.2 V). The two discharge plateaus gave a capacity of 65 mAh/g, which is about 98 % of the theoretical capacity of poly (Qz-S-EPE). After 500 cycles, the two discharge plateaus were well-preserved and the capacity retention is 74 % (Figure 22b). The cycling stability is thus significantly improved compared to that of the $Q(CF_3)_2$-pEDOT based LIB. The improved stability is attributed to the improved redox matching between the pEDOT conducting region and Qz redox potential upon Li^+-cycling. The sufficient conductance ensured by redox matching avoids the trapping of $LiQz^-$ radical, which guarantees the full redox conversion of Qz redox transfer.

It is worth to note that the conducting region of the poly (EPE) backbone is between -0.4 V and 0.7 V and that the Qz redox conversion upon Li^+-cycling occurs at the lower potential end of this potential region. This leaves a significant portion of the backbone conductive window (0.1 V-0.7 V) unutilized. Further studies should focus on exploring high potential redox-active pendants to reach the maximum LIB voltage output of 4 V based on poly (EPE). In addition, the conducting window of the polymer backbone could be extended by using polythiophene backbone instead of poly (EPE). The polythiophene based CRPs are expected to give a voltage output of 4.3 V.

5.4 Quinizarin cathode based protonic battery

Based on Figure 15 it is clear that both naphthoquinone (NQ) and Qz are redox matched with the pEDOT conducting region upon proton cycling (pKa=3.2). The redox conversion of NQ and Qz in MeTriHTFSI (pKa=3.2) electrolyte gives a potential difference of 0.8 V. Qz and NQ were functionalized onto an EPE backbone and used as capacity-carrying cathode and anode, respectively. The resulting NQ-EPE, and Qz-EPE (Scheme 5) were polymerized and characterized in MeTriHTFSI **(Paper IV)**.

5.4.1 Characterization of CRPs in Protic Ionic Liquids

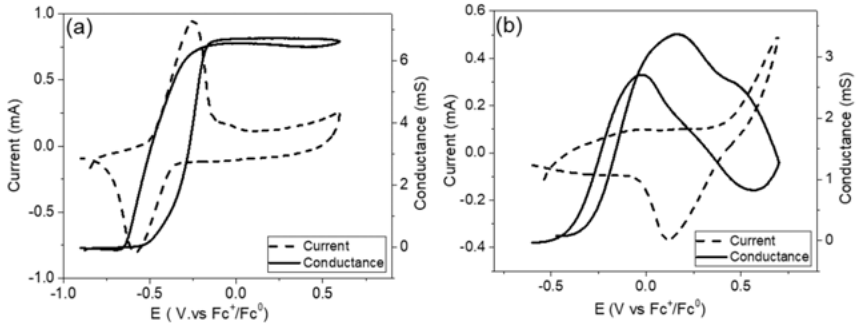

Figure 23. *In situ* conductance on IDA-Au electrode (solid line) in 0.1 M MeTriHTFSI/MeCN and cyclic voltammograms on GC (dashed line) in MeTriHTFSI of (a) poly (NQ-EPE), (b) poly (Qz-EPE) as a function of potential, performed at scan rate of 20 mV/s.

Figure 23 shows the *in situ* conductance of poly (NQ-EPE) and poly (Qz-EPE) in MeTriHTFSI. The conductance of poly (NQ-EPE) initiated from -0.5 V as the polymer is doped and reached the maximum value of 6.5 mS at -0.2 V, above which the conductance kept constant. The conductance of poly (Qz-EPE) initiated from -0.3 V as the polymer is doped and reached the maximum value of 3.5 mS at 0.15 V, however, after that the conductance decreased. Although poly (NQ-EPE) and poly (Qz-EPE) utilized the same repeating unit (EPE), the conducting threshold and conductance behavior are rather different. The higher conducting threshold of poly (Qz-EPE) compared to poly (NQ-EPE) may be attributed to the shorter poly (Qz-EPE) chain (9 EDOT units) compared to that of poly (NQ-EPE) (14 EDOT units) which was calculated according to equation 12. A longer polymer length may enhance a longer conjugation length as well as a lower onset oxidation potential.[101] It may also be attributed to charge carriers localization due to twisting of the polymer

backbone caused by the bulky quinizarin groups.[77,102,103] The decreased conductance above 0.15 V observed for poly (Qz-EPE) is attributed to the over-doping induced in-gap states depletion. Short polymers are expected to be redox active in a narrow potential window. At high potentials poly (Qz-EPE) was highly doped, causing the decrease of charge carrier concentration with conductance decreasing as a result.[104,105] The poly (NQ-EPE) chain is long enough to be redox active in a wide potential window, resulting in a conductance plateau. Cyclic voltammograms of poly (NQ-EPE) in MeTriHTFSI electrolyte showed a pair of reversible redox peaks centered at -0.35 V, which is attributed to NQ/NQH_2 redox conversion (Figure 23a). Poly (Qz-EPE) showed a pair of redox peaks centered at 0.45 V, corresponding to Qz/QzH_2 redox conversion (Figure 23b).

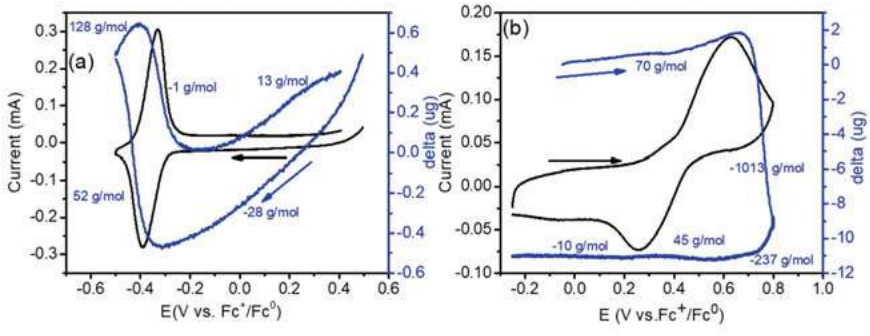

Figure 24. Cyclic voltammograms (black) and corresponding mass change (blue) of (a) 10 ug poly (NQ-EPE), (b) 10 ug poly (Qz-EPE) on EQCM-Au at a scan rate of 20 mV/s in MeTriHTFSI, the arrows indicate the start-direction of current and mass change.

Figure 24 shows the *in situ* EQCM characterization of poly (NQ-EPE) and poly (Qz-EPE) in MeTriHTFSI electrolyte. In the anodic scan of poly (NQ-EPE), an increase in mass between -0.55 V and -0.4 V was observed, which is attributed to the backbone doping-induced uptake of TFSI anion to balance the positive charge on polymer backbone. The mass increase per molar charge in this region is 128 g/mol, which is smaller than the molar weight of TFSI (280 g/mol), suggesting that proton expulsion is also involved and constitutes 54 % of the overall mass transfer. A decrease in mass between -0.4 V and -0.2 V was observed, which is attributed to the proton release from NQ/NQH_2 redox conversion. The mass decrease per molar charge in this region is -1 g/mol, which is exactly the proton molar mass (1 g/mol), suggesting that the proton expulsion is the only mass transfer process here. Above -0.2 V, the current results from the backbone doping. However, the mass increase in this region is only 13 g/mol, which is far below the molar mass of TFSI anion. It is thus concluded that proton expulsion dominated the charge balancing process and

contributed to 95 % of the overall mass transfer above -0.2 V. Worth to note is that, the poly (NQ-EPE) mass was comparatively stable with only 0.6 ug increase after one cycle (6 % of the polymer mass). In contrast, poly (Qz-EPE) experienced a huge mass decrease (about 10 ug) during the QzH_2 oxidation peak and the polymer was totally detached from current collector. This is due to the swelling of the polymer backbone, resulting from massive TFSI anion-uptake to balance the positive charge of poly (EPE) at high doping levels.

5.4.2 Battery performance evaluation

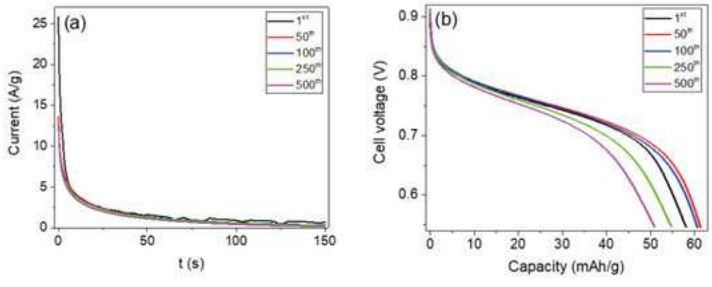

Figure 25. Battery performance with poly (NQ-EPE) as limiting material: (a) Current profile during the constant voltage charging at 1 V, (b) discharge profile of different cycles at a current density of 0.3A/g.

A proton rocking-chair battery was assembled using poly (NQ-EPE) as anode, poly (Qz-EPE) as cathode and MeTriHTFSI as electrolyte. The battery was charged by applying a constant potential and discharged at constant current. The constant voltage charging method can fully charge the battery in a short period.[106] The resulting current initially reached 25 A/g and then decreased to almost zero within 150 seconds (Figure 25a). In the subsequent constant current discharge process, the battery exhibited a discharge plateau centered at around 0.78 V (Figure 25b), which corresponds well to the potential difference between the Qz/QzH_2 and NQ/NQH_2 redox conversions in MeTriHTFSI electrolyte. Some batteries were fabricated with the cathode as limiting electrode and some with the anode as limiting electrode by varying the relative weight ratio between the two electrodes, to enable separate evaluation of the two materials in a battery configuration. Batteries with anode as limiting exhibited a discharge capacity 62 mAh/g (at 4.5 C), corresponding to 80 % of the theoretical capacity of poly (NQ-EPE) (78 mAh/g). 80 % of the capacity was retained after 500 cycles. The charging charge was calculated by integration of the current over the charging time. The coulombic efficiency is close to 100 %. For batteries with poly (Qz-EPE) as limiting material, the coulombic efficiency was only 95 % and only 75 % of the capacity was retained after 500 cycles.

5.4.3 Self-discharge and leakage current

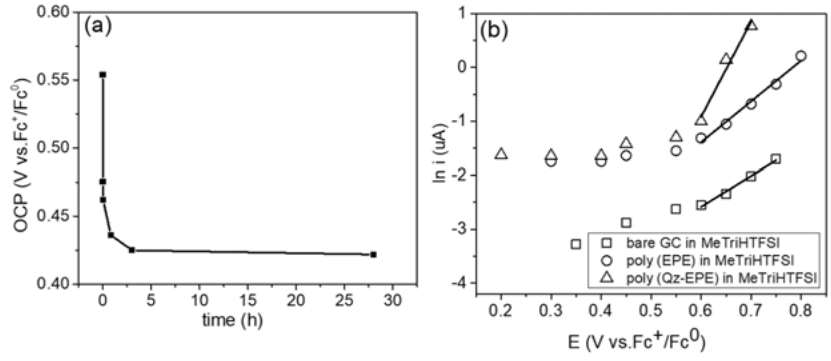

Figure 26. (a) Open circuit potential relaxation of poly (Qz-EPE) on GC in a three-electrode setup after constant voltage charging at 0.7 V for 150 s. (b) Logarithm of leakage current of bare GC (square), poly (EPE) on GC (circle), poly (Qz-EPE) on GC (triangle) as a function of applied potential in MeTriHTFSI.

A self-discharge study was conducted to investigate the origin of the low coulombic efficiency and the stability of the polymer in the charged state. Open circuit potential (OCP) relaxation was monitored on poly (Qz-EPE) electrode in a three-electrode setup. Poly (Qz-EPE) was firstly charged by applying a constant voltage at 0.7 V for 150 seconds, after which the applied voltage was removed and the OCP relaxation was monitored (Figure 26a). During the first 3 h the OCP decayed from 0.55 V to 0.43 V with 67 % of the charge retained. In the next 25 h the OCP dropped to 0.42 V with 54 % of the charge retained. This self-discharge of poly (Qz-EPE) electrode indicates that the oxidized state of Qz is unstable with respect to reduction by some reducing agents present in the system.

The low coulombic efficiency signifies loss of the charge. To be specific, either Qz/QzH_2 redox reaction or the poly (EPE) doping/dedoping is partially irreversible or other side reactions occur at high potential side. Leakage-currents were monitored to study the nature of reactions that account for the low coulombic efficiency. The leakage current of a bare GC electrode in MeTriHTFSI electrolyte increased exponentially with potential above 0.6 V (Figure 26b), indicating potential-driven oxidation of the MeTriHTFSI electrolyte. The leakage current of poly (Qz-EPE) and poly (EPE) also initiated exponentially with potential above 0.6 V, which is 0.15 V higher than the formal potential of the Qz/QzH_2 redox reaction, making Qz degradation unlikely as cause for the leakage current. The leakage current of poly (EPE) and poly (Qz-EPE) is one-order higher than that of bare GC, which could be due to the larger surface area in these GC electrodes after being covered by polymer. However, it is unlikely that the increased surface area could account for the

order-of-magnitude increase in leakage current. A more likely explanation is that irreversible oxidation (over-oxidation) of the polymer backbone dominates the current leakage. Over-oxidation is a common feature observed for conducting polymers that could be the origin of the leakage current,[107–110] We thus conclude that the low coulombic efficiency in the cathode limited battery is due to irreversible oxidation related to the poly (EPE) backbone.

.

6. Post-deposition electrochemical polymerization (PDP)

Traditional electrochemical polymerization from a monomer solution cannot fully immobilize and utilize the dissolved monomer, as most monomers remain unreacted after polymerization. In addition, this method requires that the monomer is soluble to appreciable concentrations in the electrolyte solvent used, which restricts the choice of solvent as well as the choice of electrolyte, In post-deposition polymerization (PDP), all the raw material can be utilized and there is a greater freedom of choice regarding solvent and electrolyte[31]. In the PDP method, the dissolved repeating units are deposited directly onto the electrode surface, which is then vacuum-dried to make a polymerizable film. Subsequently, the electrode is transferred to an electrolyte solution in which the repeating units do not dissolve and the film is polymerized by applying a sufficiently high potential to oxidize the repeating units.

Using trimeric repeating units can prevent dissolution-loss during polymerization and, to that end, two EDOT units were functionalized onto the ProDOT unit, synthesizing EPE structure (**Paper IV**). The trimeric structure as repeating unit can, in addition, give a lower reduction (polymerization) potential compared with the corresponding monomer (above 1 V) due to the enhanced conjugation length. The mild polymerization condition broadens the freedom to choose electrolyte systems, since many electrolytes are unstable at high polymerization potentials. The conducting nature of the trimeric structure would, in addition, facilitate electron transport within the film, which is crucial for the polymerization to occur.

6.1 Successful PDP

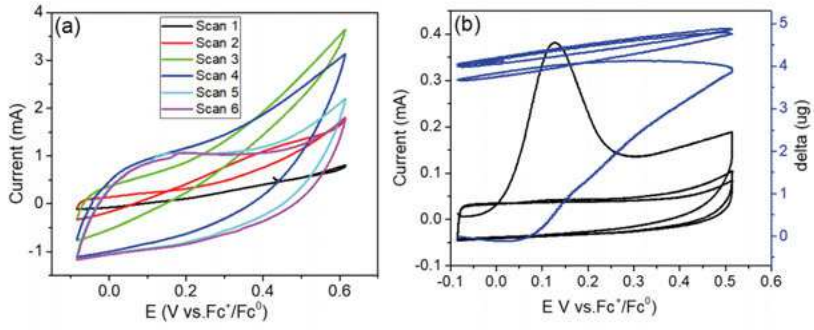

Figure 27. (a) Polymerization cyclic voltammograms of 0.5 mg NQ-EPE on GC (b) Cyclic voltammograms (black) and corresponding mass change (blue) during polymerization of 10 ug NQ-EPE on EQCM-Au electrode at 20 mV/s in 0.1 M MeTriHTFSI/MeCN/H_2O (67 % MeCN volume fraction).

NQ-EPE was dissolved in N-Methyl-2-pyrrolidone (NMP) to make a 100 mg/mL trimer solution, which was then drop-casted onto a GC current collector. NMP was then removed by vacuum drying to make a trimer film. The NQ-EPE covered electrode was transferred to a 0.1 M MeTriHTFSI/MeCN/H_2O solution (MeCN volume fraction 67 %) where NQ-EPE film did not dissolve. The trimer film was then electrochemically polymerized by CV. Figure 27a shows the polymerization cyclic voltammograms of 0.5 mg NQ-EPE layer. The current increased from 0.05 V during the first anodic scan, resulting from trimer oxidation. Subsequently, the formed trimer radical coupled to another radical, forming polymer. Meanwhile, doping/dedoping of the resulting polymer produced the capacitive current which grew upon polymeriziatiom. Polymerization was completed within 4 scans, after which only the reversible polymer doping/dedoping charge is observed as a rectangular, capacitive current response.

In situ EQCM measurements revealed an extensive mass increase above 0.05 V during CV polymerization (Figure 27b), resulting from uptake of solvent and dopant ions. In order to separate the mass change associated with solvent uptake and polymer backbone doping-induced anion uptake, we take the net mass change between the first anodic scan and cathodic scan as the solvent amount by assuming that the uptake-dopant anion in the anodic scan (doping) is reversibly expulsed during the cathodic scan (dedoping). The uptake of solvent during polymerization of NQ-EPE is 30 wt %.

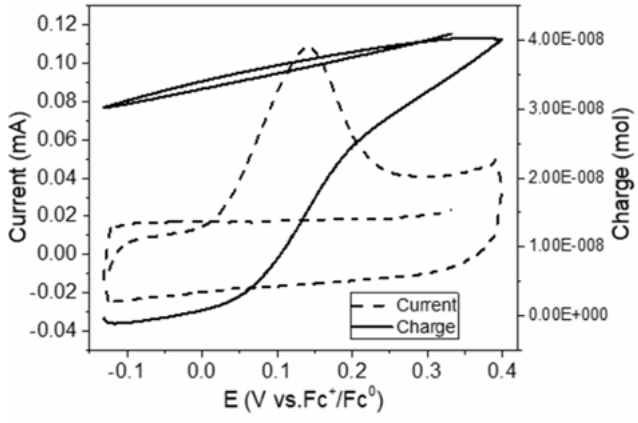

Figure 28. Cyclic voltammograms (dashed line) and charge (solid line) during polymerization of 10 ug NQ-EPE on GC electrode at a scan rate of 20 mV/s in MeTriHTFSI/MeCN/H_2O (67 % MeCN volume fraction).

The resulting polymer length after PDP was estimated from the polymerization charge. Figure 28a shows the polymerization cyclic voltammograms of 10 ug NQ-EPE ($1.3*10^{-8}$ mol). The polymerization was completed in one scan. The charge in the first anodic scan is $4.09*10^{-8}$ mol, which is the sum up of the polymerization charge and the doping charge of the resulting polymer. The doping charge can be estimated by subtracting the charge in the cathodic scan as the positively charged polymer is reversibly reduced in the cathodic scan. The dedoping charge is $2.07*10^{-8}$ mol. The estimated polymerization charge is $2.02*10^{-8}$ mol. The polymer length was calculated from the polymerization charge according to equation 12 (Section 4.2.1). The calculated average polymer length was 4.5 trimers per chain, corresponding to 14 EDOT unit. This is comparable to that found in polymers derived from traditional chemical and electrochemical polymerization methods.[111,112]

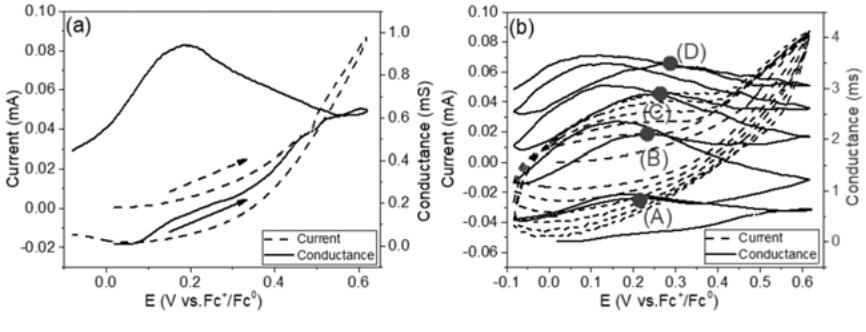

Figure 29. Conductance (solid line) and cyclic voltammograms (dashed line) during (a) the first polymerization scan, and (b) five polymerization scans of NQ-EPE on

IDA-Au electrode at 50 mV/s in 0.1 M MeTriHTFSI/MeCN/H_2O (67 % MeCN volume fraction). A, B, C, B points represents the potential where conductance reaches its maximum value in the 2nd, 3rd, 4st and 5st anodic scans.

In situ conductance measurements during polymerization shows that conductance started to increase at 0.1 V (Figure 29a). In the first cathodic scan, the conductance also increased steadily until 0.2 V due to the continuous polymerization even in the cathodic scan, which is confirmed by the irreversible positive current. Continuous polymerization produced polymer chains with increased conductance as a result. In the following anodic scan in scan 2nd the conductance initially increased as the obtained oligomer is oxidized (doped). However, further doping above 0.22 V resulted in a decreased conductance. The potential where the conductance reached the maximum value in the anodic scan is denoted as E^G_{max} here. E^G_{max} shifted positively from 0.22 V in second anodic scan (A in Figure 29b), to 0.24 V, 0.27 V and 0.28 V in third, fourth and fifth anodic scan, respectively (point B, C and D, respectively, in Figure 29b). The decreased conductance at potentials above E^G_{max} is attributed to the over-doping of the short polymer chains. Short polymers are expected to be redox active in a narrow potential window and thus can reach their maximum doping level at a relatively lower potential compared to that of a longer polymers. Over-doping results in the depletion of electrons close to the lower in-gap state and thus decreases the conductance. In this situation a maximum conductance is expected at medium doping level where half of the states have a free electron and half of the states are empty.[105] The positive-shift of E^G_{max} potential indicates that the polymer length increased with continuous polymerization. The increased polymer length is also manifested in the appearance of a conductance plateau in the fifth scan,[100] *i.e.* the conductance reached the maximum value and kept the constant value with further doping. To summarize, the phenomenon that the conductance decreased for short polymers at certain potential during the anodic scan was relieved with the formation of longer polymer chains during the subsequent polymerization scans. The over-doping induced conductance decrease almost disappeared in the fifth polymerization scan with the appearance of a conductance plateau (Figure 29b).

6.2 PDP solution optimization

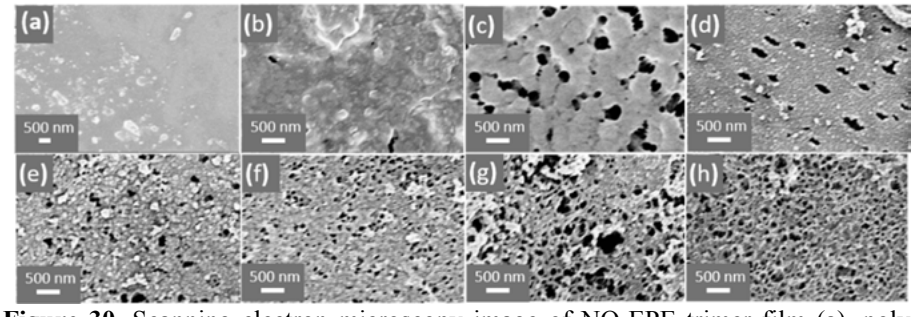

Figure 30. Scanning electron microscopy image of NQ-EPE trimer film (a), poly (NQ-EPE) polymerized in 0.1 M MeTriHTFSI/MeCN/H_2O electrolyte with (b) 0 %, (c) 25 %, (d) 33 %, (e) 50 %, (f) 67 %, (g) 75 %, (h) 100 % MeCN by volume.

Traditional polymerization process from a dissolved monomer solution involves: radical formation, dimerization, deprotonation, oligomerization, nucleation, deposition, growth and solid-state formation. The polymer length is largely determined by the polymer solubility as chain propagation termination often occurs by precipitation. In PDP, the initial state is an insoluble solid-state trimer. Since the polymerization relies on the coupling of a radical at the α-position of another radical successful polymerization in the above 0.1 M MeTriHTFSI/MeCN/H_2O (67 % MeCN volume fraction) suggests that certain kind of rearrangement is necessary to occur in order to find the coupling point. We hypothesize the rearrangement is attributed to the dissolution of intermediate, trimer radical cation since the neutral state trimer is insoluble.

Rearrangement of the trimer radical cation likely requires some solubility of the trimer in the electrolyte. In order to study the solvent effect on the trimer radical cation rearrangement during the PDP, the solvent composition was systematically varied (**Paper IV)**. In the neutral state the NQ-EPE trimer does not dissolve in H_2O while it dissolves in MeCN. When the MeCN volume fraction in the MeCN/H_2O solvent mixture is above 67 % partial dissolution of the neutral state NQ-EPE is observed. A series of 0.1 M MeTriHTFSI/MeCN/H_2O electrolytes with MeCN volume fractions of 0 %, 25 %, 33 %, 50 %, and 67 % were used as polymerization electrolytes. Figure 30a shows that the trimer layer had a smooth and dense surface. The polymerization in 0 % MeCN electrolyte produced rough, but still non-porous surface (Figure 30b). With increased MeCN volume fraction in the polymerization solution, the size of condensed aggregates decreased and became nanoparticles or nanowires. For example, the 500 nm aggregates from 25 % MeCN solution turned into 100 nm nanoparticles in 50 % MeCN (Figure 30e). In 67

% MeCN, some nanowires formed with the width of 60 nm (Figure 30f). Further increasing the MeCN volume fraction in the polymerization solution produced only nanowires.

The morphology of the resulting polymers is clearly dependent on the composition of the polymerization solvent. The observed morphology change was a result of trimer radical cation rearrangement in response to dissolution, which is dependent on the polymerization solvent composition. The rearrangement of trimer radical cation boosted the possibility to find the coupling point, facilitating the prolongation of the resulting polymer. Table 2 shows the polymer length increased with the MeCN volume fraction in the polymerization solution as expected

Table 2. Polymerization data of 10 ug NQ-EPE polymerized in 0.1 M MeTriHTFSI/MeCN/H_2O with different MeCN volume fractions.

MeCN volume fraction	**0 %**	**25 %**	**33 %**	**50 %**	**67 %**
number of trimer (mol)	$1.30*10^{-8}$	$1.30*10^{-8}$	$1.30*10^{-8}$	$1.30*10^{-8}$	$1.30*10^{-8}$
oxidative charge (mol C)	$2.95*10^{-8}$	$4.07*10^{-8}$	$3.91*10^{-8}$	$4.68*10^{-8}$	$4.09*10^{-8}$
reductive charge (mol C)	$1.74*10^{-8}$	$2.52*10^{-8}$	$2.13*10^{-8}$	$2.76*10^{-8}$	$2.07*10^{-8}$
polymerization charge (mol C)	$1.21*10^{-8}$	$1.54*10^{-8}$	$1.78*10^{-8}$	$1.92*10^{-8}$	$2.02*10^{-8}$
average polymer length (trimer)	1.9	2.5	3.2	3.8	4.5
number of EDOT unit per chain	6	8	10	11	14

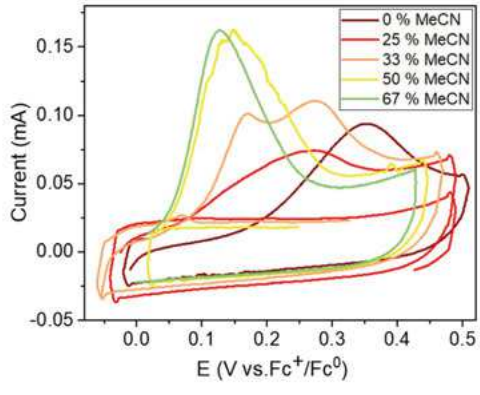

Figure 31. Polymerization cyclic voltammograms of 10 ug NQ-EPE on GC at 8 mV/s in 0.1 M MeTriHTFSI/MeCN/H_2O with different MeCN volume fractions.

Figure 31 shows the polymerization cyclic voltammograms of 10 ug NQ-EPE in 0.1 M MeTriHTFSI/MeCN/H_2O with different MeCN volume fractions. The anodic peak in the first scan is attributed to the oxidation (polymerization) of the neutral state trimer. The rectangular-shape capacitive current in

the cathodic scan is attributed to the dedoping of the resulting polymer. The polymerization was completed in one scan and only the polymer doping current is observed in the second anodic scan. The trimer oxidation peak shifted negatively with increased MeCN volume fraction. To be specific, the polymerization peak shifted from 0.35 V in 0 % MeCN to 0.12 V in 67 % MeCN. The negatively shifted oxidation peak suggests that either the neutral state trimer became unstable or the oxidized species trimer radical cation was stabilized with the increased MeCN volume fraction. The neutral state trimer layer is insoluble in the above solutions, thus has identical energy in the above polymerization solutions with different MeCN volume fractions. The negatively shifted trimer oxidation potential is thus attributed to the stabilized trimer radical cation by the solvent as a result of dissolution. Higher MeCN faction can dissolve and rearrange the trimer radical cation to a larger extent, in agreement with the hypothesis that the rearrangement of trimer radical cation facilitates the formation of porous structure and polymer chain prolongation. We thus propose the polymerization mechanism for PDP that includes 1) oxidation of the neutral trimer, 2) dissolution of radical cations, 3) radical-radical coupling, and 4) re-deposition of oligomers.

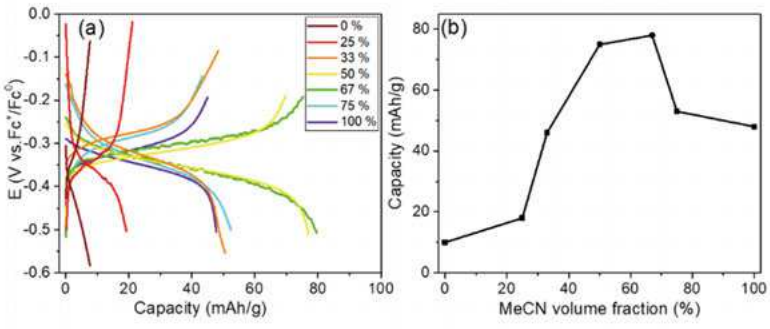

Figure 32. (a) Galvanostatic charge-discharge curves of poly (NQ-EPE) tested on GC in three-electrolyte setup in MeTriHTFSI electrolyte at a current density of 0.3 A/g, (b) corresponding discharge capacity of poly (NQ-EPE) as a function of MeCN volume fraction in the 0.1 M MeTriHTFSI/MeCN/H_2O polymerization solution.

The resulting poly (NQ-EPE) was characterized in MeTriHTFSI electrolyte by galvanostatic charge-discharge at a current density of 0.3 A/g. Poly (NQ-EPE) shows a discharge plateau centered at -0.35 V (Figure 32a), which is attributed to the NQ/NQH_2 redox conversion. The discharge capacity of poly (NQ-EPE) is strongly affected by the solution composition of polymerization electrolyte. Specifically, the discharge capacity of poly (NQ-EPE) in MeTriHTFSI increased with MeCN volume fraction in the 0.1 M MeTriHTFSI/MeCN/H_2O polymerization solution and reached the maximum value of 78 mAh/g at a MeCN volume fraction of 67 % (Figure 32b). The obtained

capacity of 78 mAh/g corresponds to 100 % of the NQ/NQH_2 theoretical capacity. Further increasing the MeCN volume fraction caused a decrease of the discharge capacity, which is attributed to dissolution loss of neutral state trimer during PDP process. In summary, a certain amount of MeCN in the polymerization solution can dissolve and rearrange the oxidized species trimer radical cation. The solvent stabilization effect on trimer radical cation caused a negative-shift of the polymerization potential. The trimer radical rearrangement enhanced nano-structuring morphology formation and polymer prolongation. The increased capacity is the result of improved electronic transport due to long polymers and improved ionic transport due to nano-structuring morphology. The optimized polymerization solution is thus 67 % MeCN for NQ-EPE.

7. Concluding remarks

The aim of the thesis was to understand Quinone-based CRPs with the long-term target to develop high-performance organic batteries in place of existing battery techniques. Quinones, as popular energy storage materials, suffer from problems related to dissolution and limited electronic conductance. Functionalizing quinones onto conducting polymer backbones to make a CRP, cannot only effectively solve dissolution problem, but also provide conductance to sustain the quinone redox reaction and, hence, to eliminate the need for conducting additives.

In this thesis pEDOT was used as the conducting agent of CRP. The basic requirement to make a quinone-pEDOT based CRP is that the formal potential of the quinone redox reaction is within the conducting region of pEDOT. The conducting region of pEDOT was relatively stable with respect to the nature of electrolyte while quinone redox potential is highly dependent on the nature of the electrolyte. The effect of cycling ion, solvent and substituent was studied experimentally as well as with DFT calculation with respect to the quinone redox chemistry. It was found that the charge-compensating cation from the electrolyte had a pronounced effect on the quinone redox potential through stabilization of the Q^{-} and Q^{2-}. Cycling a non-coordinating TBA^{+} ion showed the lowest formal potential. Cycling of coordinating Li^{+} ions showed an intermediate formal potential, while cycling of coordinating H^{+} ions showed the highest formal potential. DFT calculation showed that the Li^{+} and H^{+} bonded to Q^{-} and Q^{2-} could effectively decrease the electron density on quinone aromatic ring and stabilize the system. The cycling ion also affected the separation between the first and the second redox peaks. Cycling of non-coordinating TBA^{+} ions showed two well-separated reduction peaks. Cycling of coordinating Li^{+} showed two closely lying reduction peaks. Cycling of coordinating H^{+} showed only one redox peak. DFT calculation showed that the coulombic repulsion between two successive injected charges, is the highest, intermediate and the lowest for TBA^{+}-cycling, Li^{+}-cycling and H^{+}-cycling. In addition, the effect of substitution on the quinone redox potential was studied in seven different quinones which were substituted by $-2C(CH_3)_3$, $-C(CH_3)_3$, $-CH_3$, -F, -2F and $-2CF_3$. The formal potential for the quinone redox reaction was found to shift positively with the electron-withdrawing ability of the substituent in MeCN electrolyte. However, in aqueous electrolyte the dependence of formal potential on substituent was found to be only applicable for electron-donating substituents and disappeared with electron-withdrawing substituents.

DFT calculation showed that solvent water molecules donated electron density to the quinone aromatic system, thus offsetting electron-withdrawing effect of the substituent.

The formal potentials of -F, -2F and -2CF_3 substituted quinones upon Li^+-cycling were expected to be within the pEDOT conducting region. However, when investigating the CRPs, it was found that the conductance of CRPs was severely delayed compared to pEDOT. *In situ* UV-vis, *in situ* EQCM and *in situ* EPR, on the other hand, showed that onset doping potential of pEDOT backbone, on the other hand, was largely unaffected by the substituent. The onset of the conductance of CRPs was correlated to the $Li_2Q/LiQ^{\cdot}$ formal potential, and it was therefore concluded that the interplay between the pEDOT backbone and lithiated reduced state quinone caused the conductance threshold and conductance delay. Doping of the CRPs indeed produced charge carriers which were, however, localized by the lithiated reduced state quinone.

The high redox potential $Q(CF_3)_2$-pEDOT showed promising electrochemical performance and was thus used to assemble a LIB battery. The battery, however, showed only 67 % capacity retention after 200 cycles due to the inadequate electron transport pathways resulting from loss of redox matching. The CF_3-substituted quinone was therefore replaced by a high potential Qz pendant. The Qz showed perfect redox matching with pEDOT upon Li^+-cycling and a Qz based CRPs LIB exhibited a capacity retention of 74 % after 500 cycles. The high capacity retention confirmed the feasibility of the CRP concept to make a stable, conducting additive-free sustainable battery.

The quinone-CRP concept is feasible not only for Li^+-cycling, but also for H^+-cycling. The utilization of a Qz cathode and NQ anode gave a battery with a voltage output of 0.8 V in protonic MeTriHTFSI electrolyte. An all-organic CRPs based proton battery was assembled and showed a capacity retention of 80 % after 500 cycles.

PDP was used as an alternative to traditional electrochemical polymerization from a dissolved monomer solution. A trimer was used as the polymeric repeating unit instead of a monomer. The solvent composition in the polymerization solution was found to affect the properties of resulting polymer extensively. Increasing the MeCN volume fraction in the aqueous polymerization solution can dissolve and reorganize the trimer radical cation, which facilitates the formation of longer polymer chains, enhancing the electronic and ionic transport of the resulting polymer. In fact, it was shown that trimer rearrangement is crucial for the PDP process.

Within this thesis it is shown that redox matched quinone-pEDOT based CRPs provide a viable alternative for organic energy storage systems, *e.g.* the use of quinone pendant enables proton batteries as well as LIBs. Other cycling chemistries, such as Na^+, Ca^{2+}, Al^{3+} are worth to be explored as well as other high potential capacity-carrying cathode pendants. Other conducting polymer backbone with wide doping window is also worth to investigate so as to broaden the conducting window.

8. Svensk sammanfattning

Syftet med avhandlingen var att förstå kinonbaserade CRPs med ett långsiktigt mål att utveckla högpresterande organiska batterier. kinonbaserade CRPs förväntas byta ut traditionella batteritekniker som förlitar sig på oorganiska mineraler och därmed är dyra och har ett högt CO_2-avtryck under råmaterial extraheringen. Organiska energilagringsmolekyler, kinoner i denna avhandling, är vanligtvis lätta, har en hög specifik kapacitet, snabba redoxreaktioner och finns i en strukturell mångfald. Men kinoner som energilagringsmaterial begränsas av upplösning i elektrolyten och har en begränsad ledningsförmåga som måste avhjälpas med ledningsadditiv. Funktionalisering av ledande polymerer med kinoner som sidogrupper för att skapa CRP-material kan inte bara lösa upplösningsproblematiken utan också ge ledningsförmåga för kinonens redoxreaktion. Detta ger ett material som är fritt från additiv.

i denna avhandling har pEDOT använts som ledande polymer i CRP-material. Det grundläggande kravet för att framställa kinonfunktionaliserade -CRPs är att den formella potentialen för kinonens redoxreaktion måsta vara inom det ledande området för polymeren. Ledningsregionen för pEDOT var relativt stabil med avseende på elektrolytens sammansättning. Således måste kinonens redoxkemi förstås, vilken undersöktes i detalj: Effekten av cyklingsjon, lösningsmedel och substitutioner på kinonringen studerades experimentellt såväl som med DFT-beräkningar. Det visade sig att den laddningskompenserande katjonen hade en uttalad effekt på kinonens redoxpotential genom stabilisering av semikinonens radikalanjon och den reducerade kinonens dianjon. Cykling av icke-koordinerande TBA^+ visade den lägsta formella potentialen, medan cykling av Li^+, vilken koordinerar till kinonens syre, visade en högre formell potential. Vidare kunde cykling av H^+, vilken binder med kovalent styrka till syret, en starkare bindning än både okoordinerad och koordinerad jonbindning, visa på den högsta formella potentialen. DFT-beräkningar visade att Li^+ och H^+ är bundna till semikinonen medan den reducerade kinonen fick minskade elektrondensiteter på kinonens aromatiska ring vilket stabiliserade systemet. Cyklingsjonen påverkade också toppseparation mellan den första och den andra redoxprocessen. Cykling av icke-koordinerande TBA^+ visade två reduktionstoppar som var i stort sett separerade. Cykling av koordinerande Li^+ visade två reduktionstoppar som var delvis separerade. Cykling av koordinerande H^+ visade bara en reduktionstopp. DFT-beräkningar visade att den coulombiska repulsionen mellan de två efterpåföljande laddningsprocesserna är den högsta, mellanliggande och lägsta för

TBA^+ cykling, Li^+ cykling och H^+ cykling. Dessutom, redoxpotentialens påverkan av substitution på kinonringen studerades på sju olika kinoner substituerade med $-2C(CH_3)_3$, $-C(CH_3)_3$, $-CH_3$, -F, -2F och $-2CF_3$. Den formella potentialen av kinonens redoxreaktion visade sig förändras positivt med elektrondragande substitution i MeCN-elektrolyt. I vattenhaltig elektrolyt var påverkan från substitutioner endast uttalade för elektrondonerande substitutioner och försvann vid elektrondragande substitution. DFT-beräkningar visade att vatten som lösningsmedel donerade elektrondensitet till kinonens aromatiska system, vilket kompenserade effekten av elektrondragande substitutioner.

När kinonen är substituerad med -F, -2F och $-2CF_3$, är den formella potentialen vid Li^+ cykling inom det ledande området hos PEDOT, dock minskade fönstret för ledningsförmågan avsevärt hos CRPs jämfört med PEDOT. Från In situ UV-vis, in situ EQCM och in situ EPR, ses att potentialen för dopningsonset inte påverkas av substitutionen. Onset för ledningsförmågan hos CRPs korrelerade väl med den formella potentialen av $Li_2Q/LiQ^{\cdot}$. Därmed dras således slutsatsen att samspelet mellan pEDOT skelettet och det litierade tillståndet hos en reducerad kinon orsakade den fhöga tröskeln för ledningsförmågan och ledningsfördröjningen. Dopning av CRPs producerar laddningsbärare, vilka dock lokaliseras av den litierade kinonen.

$Q(CF_3)_2$-pEDOT visade lovande elektrokemisk prestanda, så detta material användes för att tillverka ett Li-batteri. Batteriet visade emellertid endast 67 % bibehållen kapacitet efter 200 cykler. den låga stabiliteten tillskrivs den otillräckliga elektrontransporten på grund av förlorad redoxmatchning, därför användes vidare högpotential-quinizarin för att förbättra redoxmatchningen. Quinizarinen visade fullständig redoxmatchning med pEDOT vid Li^+ cykling. Quinizarin-baserade CRP-LIB uppvisade 74 % bibehållen kapacitet efter 500 cykler. Den höga cyklingsstabiliteten bekräftade möjligheteten med CRP-konceptet: att göra ett stabilt, ledande och additivfritt batteri.

CRP-konceptet baserat på kinoner används inte bara för Li^+ cykling, utan också för H^+ cykling. Användningen av quinizarin-katoden och naftokinon-anoden gav en batterispänning av 0.8 V i protisk MeTriHTFSI-elektrolyt. Ett helt organiskt CRP-baserat protonbatteri tillverkades som visade 80 % bibehållen laddningskapacitet efter 500 cykler.

Post-deposit elektorpolymerisationsmetoden användes som ett alternativ till traditionell elektropolymerisering från en upplöst monomerlösning. En olöslig trimer användes som en upprepande enhet för polymeren. Lösningsmedelskompositionen i polymerisationslösningen befanns påverka egenskaperna hos resulterande polymer. tillsats av MeCN i den vattenhaltiga polymerisationslösningen kan omorganisera trimerens radikalkatjon och underlätta bildandet av en lång polymerkedja medhar bra elektroniska och joniska transportegenskaper. omlagring av trimerens radikalkatjon är viktig för PDP-processer.

Inom denna avhandling har jag visat att redoxmatchade kinonbaserade CRPs ger ett möjligt alternativ för organiska energilagringssystem. Användning av kinoner kan användas för protonbatterier såväl som för LIB. Andra cyklingskemier, till exempel Na^{+}, Ca^{2+}, Al^{3+}, är värda att utforskas såväl som stabila katoder med hög potential. Andra ledande polymerskelett med hög dopningsnivå är också värda att undersökas för att bredda ledningsfönstret.

9. Acknowledgement

I would like to thank everyone who appeared in my life in the past four years. Thank you for making my PhD life in Sweden more colorful and meaningful than I expected as well as the confidence and happiness I gained from you all. First of all, I would like to deeply thank my main supervisor Prof. *Martin Sjödin*. Thank you for recruiting me who almost was freshman on electrochemistry and had an obscured understanding about scientific research as a member in this group. I really enjoy the discussion time with you on fundamental experiments. I also appreciate your attitude towards research, which affected me a lot during the last four years. Hopefully, it will continue in my whole academic life if I continue on this road. I would also thank my co-supervisor Dr. *Rikard Emanuelsson* for compounds you synthesized as well as all the off-work time you spent on discussing my experiments and follow-up study. I am quite impressed by all your encouragement and support to conduct the experiments I was interested in. I enjoy the time to discuss with you about popular organic battery using our CRP concepts.

I would also thank my co-supervisor Prof. *Maria Strømme* for all the experimental instruments you provided. I was depressed by your detailed interpretation on impedance. I would also thank all the collaboration. Prof. *Fikret Mamedov* for your support to conduct and analysis EPR experiment as well as share your interesting experience in Soviet Union. Dr. *Haidong* for your help with endless pouch cell assembling as well as your timely help when I was sick. Dr. *Amitava Banerjee* for your help with DFT calculation.

In the battery group for the past and present students I have worked with, thank you *Mia* to be a sweet girl to help me on experiments as well as your help to understand my project better. I would also thank you to share a lot Swedish culture when we were roommate as well as your caring during my dark day in office. Thank you *Lisa* for all the fika and office talks with you. I enjoy the happy roommate time in GRC and drinking time in organic battery days with you. I also like all the cute stories you shared about Sixten. Thank you *Christian* to be the temporary engineer on endless glovebox and crushed autolab laptop problems. Thank you for all happiness you brought during boring experimental time. I really enjoy the time on conference with you to hang out for nice food and to be the driver. I want to thank *Felicia* and *Rebecka* for all the interesting talks during lunch time and the interesting discussions in lab. I also want to thank *Li* for answering a lot of questions before I come to Uppsala as well as help me a lot on *in situ* experiment. I also want to thank

Hao and Oka for all the interesting talks in lab. I want give special thanks to *Xiao* for your help in understanding organic chemistry as well as take me to visit the organic lab. I also want to sincerely thank you and *Cuiyan* for caring when I was a freshman here. I will always remember all the interesting trips, dinners and movie times.

Every NMFers who in some kind of way support me. Thank you: *Xueying Chao, Shengyang, Lulu, Jonaton, Ingrid, Jörgen, Leven, Ken, Natalia, Jonas, Teresa, Ocean, Petter, Carlos, Albert*, *Evgenii, Michelle, Ribooga, Anna, Christos, Dario Martín, Maxim, Johan.* I would also thank all the past colleagues in NMF: *Rui&Lei, Jiaojiao&Jun Luo, Changqing, Peng&Yan, Jun Liu, Pengfei*. Thank you for all your support and many dinners, trips, and games as well as to be looked after like a younger sister.

I also want to thank my friends who make my life out of lab meaningful. Thank you *Xingxing, Yayuan* and *Pei* for all your support to go through my hard times and share the joys, endless girls party times, dinners, trips and games. Thank you *Yang* and *Xiaofeng* for all your encouragement, generous sharing and happy dinner times. Thank you *Rabia* for all the fika, running and shopping times. Thank *Xi, Pianpian* and *Wenjuan* for teaching me how to swim. *Thank Shuangshuang* and *Shiyu* for the happy badminton times. *Thank Qitao* and *Chiao- Wei* for helping me understand physics related questions. Thank *Zhenhua, Xin, Yingtao, Yuan, Chenyu, Bei, Zhaohui, Xiaoyong, Litao, Zhigang, Tianbo, Yawen, Hua, Ye, Si, Libo, Ruijun&Qiuhong, Zhen, Lichuan, Shihuai, Jinbao, Chenjuan, Hailiang, Jie, Jingjing, Huiying, Yujia, Yanan, Zhiwei, Shiyang, Fawad and Cecilia* for all the dinners, trips, games and joys. I am so lucky to meet you all here. I want to give special thanks to *Yanyan* for your companying and endless dinners during the first year here, I am happy to meet you here and become close friends since then.

I would specially like to thank China Scholarship Council for the financial support for my PhD study. Thank Anna Maria Lundins Foundation, Åforsk foundation, liljeforsgatan foundation, Ericssion foundation for your financial support to conference.

Finally, I would like to thank my friends *Xinpei, Ke, Bing, Haiming, Nian, Xiaodan, Yilei* and many others for all your joy and caring from China. Many thanks to my parents, brother, sister and aunt for your love, support, encouragement and understanding.

10. Reference

(1) Lewis, N. S. Powering the Planet. *MRS Bull.* **2007**, *32* (10), 808–820. https://doi.org/10.1557/mrs2007.168.

(2) Yoshino, A. The Birth of the Lithium-Ion Battery. *Angew. Chem. Int. Ed.* **2012**, *51* (24), 5798–5800. https://doi.org/10.1002/anie.201105006.

(3) Larcher, D.; Tarascon, J.-M. Towards Greener and More Sustainable Batteries for Electrical Energy Storage. *Nature Chem* **2015**, *7* (1), 19–29. https://doi.org/10.1038/nchem.2085.

(4) Elgrishi, N.; Rountree, K. J.; McCarthy, B. D.; Rountree, E. S.; Eisenhart, T. T.; Dempsey, J. L. A Practical Beginner's Guide to Cyclic Voltammetry. *J. Chem. Educ.* **2018**, *95* (2), 197–206. https://doi.org/10.1021/acs.jchemed.7b00361.

(5) Stromme, M.; Niklasson, G. A.; Granqvist, C. G. VOLTAMMETRY ON FRACTALS. *96* (3), 4.

(6) Randles, J. E. B. A CATHODE RAY POLAROGRAPH. PART 11.-THE CURRENT-VOLTAGE CURVES. 15.

(7) Costentin, C.; Porter, T. R.; Savéant, J.-M. How Do Pseudocapacitors Store Energy? Theoretical Analysis and Experimental Illustration. *ACS Appl. Mater. Interfaces* **2017**, *9* (10), 8649–8658. https://doi.org/10.1021/acsami.6b14100.

(8) Laviron, E. GENERAL EXPRESSION OF THE LINEAR POTENTIAL SWEEP VOLTAMMOGRAM IN THE CASE OF DIFFUSIONLESS ELECTROCHEMICAL SYSTEMS. 10.

(9) Stemmet, C. P.; Schouten, J. C.; Nijhuis, T. A. In-Situ UV−Visible and Raman Spectroscopy for Gas−Liquid−Solid Systems. *Ind. Eng. Chem. Res.* **2009**, *48* (17), 8205–8210. https://doi.org/10.1021/ie801984w.

(10) Calvo, E. J.; Etchenique, R. A. Kinetic Applications of the Electrochemical Quartz Crystal Microbalance (EQCM). In *Comprehensive Chemical Kinetics*; Elsevier, 1999; Vol. 37, pp 461–487. https://doi.org/10.1016/S0069-8040(99)80017-X.

(11) Karlsson, C.; Huang, H.; Strømme, M.; Gogoll, A.; Sjödin, M. Ion- and Electron Transport in Pyrrole/Quinone Conducting Redox Polymers Investigated by In Situ Conductivity Methods. *Electrochimica Acta* **2015**, *179*, 336–342. https://doi.org/10.1016/j.electacta.2015.02.193.

(12) Hannan, M. A.; Hoque, Md. M.; Hussain, A.; Yusof, Y.; Ker, P. J. State-of-the-Art and Energy Management System of Lithium-Ion Batteries in Electric Vehicle Applications: Issues and Recommendations. *IEEE Access* **2018**, *6*, 19362–19378. https://doi.org/10.1109/ACCESS.2018.2817655.

(13) Abruña, H. D.; Kiya, Y.; Henderson, J. C. Batteries and Electrochemical Capacitors. *Physics Today* **2008**, *61* (12), 43–47. https://doi.org/10.1063/1.3047681.

(14) Wakihara, M. Recent Developments in Lithium Ion Batteries. *Materials Science and Engineering: R: Reports* **2001**, *33* (4), 109–134. https://doi.org/10.1016/S0927-796X(01)00030-4.

(15) Dong, H.; Liang, Y.; Tutusaus, O.; Mohtadi, R.; Zhang, Y.; Hao, F.; Yao, Y. Directing Mg-Storage Chemistry in Organic Polymers toward High-Energy Mg Batteries. *Joule* **2019**, *3* (3), 782–793. https://doi.org/10.1016/j.joule.2018.11.022.

(16) Oka, K.; Kato, R.; Oyaizu, K.; Nishide, H. Poly(Vinyldibenzothiophenesulfone): Its Redox Capability at Very Negative Potential Toward an All□Organic Rechargeable Device with High□Energy Density. *Advanced Functional Materials* **2018**, *28* (50), 1805858. https://doi.org/10.1002/adfm.201805858.

(17) Chen, H.; Armand, M.; Courty, M.; Jiang, M.; Grey, C. P.; Dolhem, F.; Tarascon, J.-M.; Poizot, P. Lithium Salt of Tetrahydroxybenzoquinone: Toward the Development of a Sustainable Li-Ion Battery. *Journal of the American Chemical Society* **2009**, *131* (25), 8984–8988. https://doi.org/10.1021/ja9024897.

(18) Muench, S.; Wild, A.; Friebe, C.; Häupler, B.; Janoschka, T.; Schubert, U. S. Polymer-Based Organic Batteries. *Chemical Reviews* **2016**, *116* (16), 9438–9484. https://doi.org/10.1021/acs.chemrev.6b00070.

(19) Liang, Y.; Luo, C.; Wang, F.; Hou, S.; Liou, S.-C.; Qing, T.; Li, Q.; Zheng, J.; Cui, C.; Wang, C. An Organic Anode for High Temperature Potassium-Ion Batteries. *Advanced Energy Materials* **2019**, *9* (2), 1802986. https://doi.org/10.1002/aenm.201802986.

(20) NuLi, Y.; Guo, Z.; Liu, H.; Yang, J. A New Class of Cathode Materials for Rechargeable Magnesium Batteries: Organosulfur Compounds Based on Sulfur–Sulfur Bonds. *Electrochemistry Communications* **2007**, *9* (8), 1913–1917. https://doi.org/10.1016/j.elecom.2007.05.009.

(21) Visco, S. J. A Novel Class of Organosulfur Electrodes for Energy Storage. *J. Electrochem. Soc.* **1989**, *136* (3), 661. https://doi.org/10.1149/1.2096706.

(22) Deng, S.-R.; Kong, L.-B.; Hu, G.-Q.; Wu, T.; Li, D.; Zhou, Y.-H.; Li, Z.-Y. Benzene-Based Polyorganodisulfide Cathode Materials for Secondary Lithium Batteries. *Electrochimica Acta* **2006**, *51* (13), 2589–2593. https://doi.org/10.1016/j.electacta.2005.07.045.

(23) Nishide, H.; Iwasa, S.; Pu, Y.-J.; Suga, T.; Nakahara, K.; Satoh, M. Organic Radical Battery: Nitroxide Polymers as a Cathode-Active Material. *Electrochimica Acta* **2004**, *50* (2–3), 827–831. https://doi.org/10.1016/j.electacta.2004.02.052.

(24) Bugnon, L.; Morton, C. J. H.; Novak, P.; Vetter, J.; Nesvadba, P. Synthesis of Poly(4-Methacryloyloxy-TEMPO) via Group-Transfer Polymerization and Its Evaluation in Organic Radical Battery. *Chem. Mater.* **2007**, *19* (11), 2910–2914. https://doi.org/10.1021/cm063052h.

(25) Pirnat, K.; Dominko, R.; Cerc-Korosec, R.; Mali, G.; Genorio, B.; Gaberscek, M. Electrochemically Stabilised Quinone Based Electrode Composites for Li-Ion Batteries. *Journal of Power Sources* **2012**, *199*, 308–314. https://doi.org/10.1016/j.jpowsour.2011.10.068.

(26) Song, Z.; Qian, Y.; Liu, X.; Zhang, T.; Zhu, Y.; Yu, H.; Otani, M.; Zhou, H. A Quinone-Based Oligomeric Lithium Salt for Superior Li–Organic Batteries. *Energy Environ. Sci.* **2014**, *7* (12), 4077–4086. https://doi.org/10.1039/C4EE02575J.

(27) Zhong, M.; Guan, J.; Feng, Q.; Wu, X.; Xiao, Z.; Zhang, W.; Tong, S.; Zhou, N.; Gong, D. Accelerated Polysulfide Redox Kinetics Revealed by Ternary Sandwich-Type S@Co/N-Doped Carbon Nanosheet for High-Performance Lithium-Sulfur Batteries. *Carbon* **2018**, *128*, 86–96. https://doi.org/10.1016/j.carbon.2017.11.084.

(28) Katsumata, T.; Satoh, M.; Wada, J.; Shiotsuki, M.; Sanda, F.; Masuda, T. Polyacetylene and Polynorbornene Derivatives Carrying TEMPO. Synthesis and Properties as Organic Radical Battery Materials. *Macromol. Rapid Commun.* **2006**, *27* (15), 1206–1211. https://doi.org/10.1002/marc.200600286.

(29) Song, Z.; Qian, Y.; Liu, X.; Zhang, T.; Zhu, Y.; Yu, H.; Otani, M.; Zhou, H. A Quinone-Based Oligomeric Lithium Salt for Superior Li–Organic Batteries. *Energy Environ. Sci.* **2014**, *7* (12), 4077–4086. https://doi.org/10.1039/C4EE02575J.

(30) Wang, X.; Shang, Z.; Yang, A.; Zhang, Q.; Cheng, F.; Jia, D.; Chen, J. Combining Quinone Cathode and Ionic Liquid Electrolyte for Organic Sodium-Ion Batteries. *Chem* **2019**, *5* (2), 364–375. https://doi.org/10.1016/j.chempr.2018.10.018.

(31) Dong, X.; Chen, L.; Liu, J.; Haller, S.; Wang, Y.; Xia, Y. Environmentally-Friendly Aqueous Li (or Na)-Ion Battery with Fast Electrode Kinetics and Super-Long Life. *Sci. Adv.* **2016**, *2* (1), e1501038. https://doi.org/10.1126/sciadv.1501038.

(32) Strietzel, C.; Sterby, M.; Huang, H.; Strømme, M.; Emanuelsson, R.; Sjödin, M. An Aqueous Conducting Redox Polymer Based Proton Battery That Can Withstand Rapid Constant□voltage Charging and Sub□zero Temperatures. *Angew. Chem. Int. Ed.* **2020**, anie.202001191. https://doi.org/10.1002/anie.202001191.

(33) Pan, B.; Zhou, D.; Huang, J.; Zhang, L.; Burrell, A. K.; Vaughey, J. T.; Zhang, Z.; Liao, C. 2,5-Dimethoxy-1,4-Benzoquinone (DMBQ) as Organic Cathode for Rechargeable Magnesium-Ion Batteries. *J. Electrochem. Soc.* **2016**, *163* (3), A580–A583. https://doi.org/10.1149/2.0021605jes.

(34) Zhao, Q.; Huang, W.; Luo, Z.; Liu, L.; Lu, Y.; Li, Y.; Li, L.; Hu, J.; Ma, H.; Chen, J. High-Capacity Aqueous Zinc Batteries Using Sustainable Quinone Electrodes. *Sci. Adv.* **2018**, *4* (3), eaao1761. https://doi.org/10.1126/sciadv.aao1761.

(35) Louis, E.; Macdiarmid, A.; Chiang, H. K. Synthesis of Electrically Conducting Organic Polymers : Halogen Derivatives of Polyacetylene, (CH),. 3.

(36) Chiang, C. K.; Fincher, C. R.; Park, Y. W.; Heeger, A. J.; Shirakawa, H.; Louis, E. J.; Gau, S. C.; MacDiarmid, A. G. Electrical Conductivity in Doped Polyacetylene. *Phys. Rev. Lett.* **1977**, *39* (17), 1098–1101. https://doi.org/10.1103/PhysRevLett.39.1098.

(37) Wang, H.; Song, Y.; Zhou, J.; Xu, X.; Hong, W.; Yan, J.; Xue, R.; Zhao, H.; Liu, Y.; Gao, J. High-Performance Supercapacitor Materials Based on Polypyrrole Composites Embedded with Core-Sheath Polypyrrole@MnMoO 4 Nanorods. *Electrochimica Acta* **2016**, *212*, 775–783. https://doi.org/10.1016/j.electacta.2016.07.035.
(38) McCullough, R. D. The Chemistry of Conducting Polythiophenes. 24.
(39) Kang, E. Polyaniline: A Polymer with Many Interesting Intrinsic Redox States. *Progress in Polymer Science* **1998**, *23* (2), 277–324. https://doi.org/10.1016/S0079-6700(97)00030-0.
(40) Macdiarmid, A. G.; Chiang, J. C.; Richter, A. F.; Epstein, A. J. Polyaniline: A New Concept in Conducting Polymers. *Synthetic Metals* **1987**, *18* (1–3), 285–290. https://doi.org/10.1016/0379-6779(87)90893-9.
(41) Bhadra, S.; Khastgir, D.; Singha, N. K.; Lee, J. H. Progress in Preparation, Processing and Applications of Polyaniline. *Progress in Polymer Science* **2009**, *34* (8), 783–810. https://doi.org/10.1016/j.progpolymsci.2009.04.003.
(42) Waware, U. S.; Hamouda, A. M. S.; Majumdar, D. Synthesis, Characterization and Physicochemical Studies of Copolymers of Aniline and 3-Nitroaniline. *Polym. Bull.* **2019**. https://doi.org/10.1007/s00289-019-02957-y.
(43) Olsson, H.; Jämstorp Berg, E.; Strømme, M.; Sjödin, M. Self-Discharge in Positively Charged Polypyrrole–Cellulose Composite Electrodes. *Electrochemistry Communications* **2015**, *50*, 43–46. https://doi.org/10.1016/j.elecom.2014.11.004.
(44) Olsson, H.; Sjödin, M.; Berg, E. J.; Strømme, M.; Nyholm, L. Self-Discharge Reactions in Energy Storage Devices Based on Polypyrrole-Cellulose Composite Electrodes. *Green* **2014**, *4* (1–6). https://doi.org/10.1515/green-2014-0003.
(45) Olsson, H.; Nyström, G.; Strømme, M.; Sjödin, M.; Nyholm, L. Cycling Stability and Self-Protective Properties of a Paper-Based Polypyrrole Energy Storage Device. *Electrochemistry Communications* **2011**, *13* (8), 869–871. https://doi.org/10.1016/j.elecom.2011.05.024.
(46) Groenendaal, L. [a]Bert[o]; Jonas, F.; Freitag, D.; Pielartzik, H.; Reynolds, J. R. Poly(3,4□ethylenedioxythiophene) and Its Derivatives: Past, Present, and Future. 14.
(47) Groenendaal, L.; Zotti, G.; Aubert, P.-H.; Waybright, S. M.; Reynolds, J. R. Electrochemistry of Poly(3,4-Alkylenedioxythiophene) Derivatives. *Adv. Mater.* **2003**, *15* (11), 855–879. https://doi.org/10.1002/adma.200300376.
(48) Sakunpongpitiporn, P.; Phasuksom, K.; Paradee, N.; Sirivat, A. Facile Synthesis of Highly Conductive PEDOT:PSS *via* Surfactant Templates. *RSC Adv.* **2019**, *9* (11), 6363–6378. https://doi.org/10.1039/C8RA08801B.
(49) Fabretto, M.; Zuber, K.; Hall, C.; Murphy, P.; Griesser, H. J. The Role of Water in the Synthesis and Performance of Vapour Phase Polymerised PEDOT Electrochromic Devices. *J. Mater. Chem.* **2009**, *19* (42), 7871. https://doi.org/10.1039/b912324e.
(50) Schoetz, T.; Ponce de Leon, C.; Bund, A.; Ueda, M. Electro-Polymerisation and Characterisation of PEDOT in Lewis Basic, Neutral and Acidic EMImCl-AlCl3 Ionic Liquid. *Electrochimica Acta* **2018**, *263*, 176–183. https://doi.org/10.1016/j.electacta.2018.01.033.

(51) Harrison, D. P.; Carpenter, L. S.; Hyde, J. T. Reductive Electropolymerization of a Vinyl-Containing Poly-Pyridyl Complex on Glassy Carbon and Fluorine-Doped Tin Oxide Electrodes. *JoVE* **2015**, No. 95, 52035. https://doi.org/10.3791/52035.

(52) Yang, L.; Mihali, V.-A.; Brandell, D.; Strømme, M.; Sjödin, M. Conjugated Pyridine-Based Polymers Characterized as Conductivity Carrying Components in Anode Materials. *J. Phys. Chem. C* **2014**, *118* (45), 25956–25963. https://doi.org/10.1021/jp509606c.

(53) Heeger, A. J.; Kivelson, S.; Schrieffer, J. R.; Su, W.-P. Solitons in Conducting Polymers. *Rev. Mod. Phys.* **1988**, *60* (3), 781–850. https://doi.org/10.1103/RevModPhys.60.781.

(54) "Synthetic Metals": A Novel Role for Organic Polymers (Nobel Lecture). *Angew. Chem. Int. Ed.* **2001**, 10.

(55) Li, X.; Jiao, Y.; Li, S. The Syntheses, Properties and Application of New Conducting Polymers. *European Polymer Journal* **1991**, *27* (12), 1345–1351. https://doi.org/10.1016/0014-3057(91)90233-E.

(56) Brédas, J. L.; Thémans, B.; Fripiat, J. G.; André, J. M.; Chance, R. R. Highly Conducting Polyparaphenylene, Polypyrrole, and Polythiophene Chains: An *Ab Initio* Study of the Geometry and Electronic-Structure Modifications upon Doping. *Phys. Rev. B* **1984**, *29* (12), 6761–6773. https://doi.org/10.1103/PhysRevB.29.6761.

(57) Chen, W.-C.; Jenekhe, S. A. Small-Bandgap Conducting Polymers Based on Conjugated Poly(Heteroarylene Methines). 2. Synthesis, Structure, and Properties. *Macromolecules* **1995**, *28* (2), 465–480. https://doi.org/10.1021/ma00106a009.

(58) Brédas, J. L.; Scott, J. C.; Yakushi, K.; Street, G. B. Polarons and Bipolarons in Polypyrrole: Evolution of the Band Structure and Optical Spectrum upon Doing. *Phys. Rev. B* **1984**, *30* (2), 1023–1025. https://doi.org/10.1103/PhysRevB.30.1023.

(59) Kaneto, K.; Yoshino, K. Electrical and Optical Properties of Polaronic States in Conducting Polymer, Polythiophene. *Synthetic Metals* **1987**, *18* (1–3), 133–138. https://doi.org/10.1016/0379-6779(87)90867-8.

(60) Rudge, A.; Davey, J.; Raistrick, I.; Gottesfeld, S.; Ferraris, J. P. Conducting Polymers as Active Materials in Electrochemical Capacitors. *Journal of Power Sources* **1994**, *47* (1–2), 89–107. https://doi.org/10.1016/0378-7753(94)80053-7.

(61) Ferraris, J. P.; Henderson, C.; Torres, D.; Meeker, D. Synthesis, Spectroelectrochemistry and Application in Electrochromic Devices of an n- and p-Dopable Conducting Polymer. *Synthetic Metals* **1995**, *72* (2), 147–152. https://doi.org/10.1016/0379-6779(94)02331-R.

(62) Kobayashi, M.; Colaneri, N.; Boysel, M.; Wudl, F.; Heeger, A. J. The Electronic and Electrochemical Properties of Poly(Isothianaphthene). *The Journal of Chemical Physics* **1985**, *82* (12), 5717–5723. https://doi.org/10.1063/1.448559.

(63) Arbizzani, C.; Catellani, M.; Mastragostino, M.; Mingazzini, C. N- and P-Doped Polydithieno[3,4-B:3′,4′-D] Thiophene: A Narrow Band Gap Polymer for Redox Supercapacitors. *Electrochimica Acta* **1995**, *40* (12), 1871–1876. https://doi.org/10.1016/0013-4686(95)00096-W.

(64) Lippe, J.; Holze, R. Electrochemical In-Situ Conductivity and Polaron Concentration Measurements at Selected Conducting Polymers. *Synthetic Metals* **1991**, *43* (1–2), 2927–2930. https://doi.org/10.1016/0379-6779(91)91208-R.

(65) Bredas, J. L.; Street, G. B. Polarons, Bipolarons, and Solitons in Conducting Polymers. *Acc. Chem. Res.* **1985**, *18* (10), 309–315. https://doi.org/10.1021/ar00118a005.

(66) Bredas, J. L.; Themans, B.; Andre, J. M.; Chance, R. R.; Silbey, R. The Role of Mobile Organic Radicals and Ions (Solitons, Polarons and Bipolarons) in the Transport Properties of Doped Conjugated Polymers. *Synthetic Metals* **1984**, *9* (2), 265–274. https://doi.org/10.1016/0379-6779(84)90064-X.

(67) Huang, H.; Karlsson, C.; Mamedov, F.; Strømme, M.; Gogoll, A.; Sjödin, M. Polaron Disproportionation Charge Transport in a Conducting Redox Polymer. *J. Phys. Chem. C* **2017**, *121* (24), 13078–13083. https://doi.org/10.1021/acs.jpcc.7b03671.

(68) Chance, R. R.; Brédas, J. L.; Silbey, R. Bipolaron Transport in Doped Conjugated Polymers. *Phys. Rev. B* **1984**, *29* (8), 4491–4495. https://doi.org/10.1103/PhysRevB.29.4491.

(69) Sterby, M.; Emanuelsson, R.; Mamedov, F.; Strømme, M.; Sjödin, M. Investigating Electron Transport in a PEDOT/Quinone Conducting Redox Polymer with in Situ Methods. *Electrochimica Acta* **2019**, *308*, 277–284. https://doi.org/10.1016/j.electacta.2019.03.207.

(70) Onoda, M.; Nakayama, H.; Morita, S.; Yoshino, K. Electrochemical Doping Properties and Electronic States of Poly(3□phenylthiophene). *Journal of Applied Physics* **1993**, *73* (6), 2859–2865. https://doi.org/10.1063/1.353013.

(71) Signifi Cant Electronic Thermal Transport in the Conducting Polymer Poly(3,4-Ethylenedioxythiophene).Pdf.

(72) Yano, H.; Kudo, K.; Marumo, K.; Okuzaki, H. Fully Soluble Self-Doped Poly(3,4-Ethylenedioxythiophene) with an Electrical Conductivity Greater than 1000 S Cm $^{-1}$. *Sci. Adv.* **2019**, *5* (4), eaav9492. https://doi.org/10.1126/sciadv.aav9492.

(73) Schulz, G. L.; Ludwigs, S. Controlled Crystallization of Conjugated Polymer Films from Solution and Solvent Vapor for Polymer Electronics. *Adv. Funct. Mater.* **2017**, *27* (1), 1603083. https://doi.org/10.1002/adfm.201603083.

(74) Huang, J.-H.; Kekuda, D.; Chu, C.-W.; Ho, K.-C. Electrochemical Characterization of the Solvent-Enhanced Conductivity of Poly(3,4-Ethylenedioxythiophene) and Its Application in Polymer Solar Cells. *J. Mater. Chem.* **2009**, *19* (22), 3704. https://doi.org/10.1039/b822729b.

(75) Pace, G.; Bargigia, I.; Noh, Y.-Y.; Silva, C.; Caironi, M. Intrinsically Distinct Hole and Electron Transport in Conjugated Polymers Controlled by Intra and Intermolecular Interactions. *Nat Commun* **2019**, *10* (1), 5226. https://doi.org/10.1038/s41467-019-13155-9.

(76) Du, Y.; Yao, H.; Galuska, L.; Ge, F.; Wang, X.; Lu, H.; Zhang, G.; Gu, X.; Qiu, L. Side-Chain Engineering To Optimize the Charge Transport Properties of Isoindigo-Based Random Terpolymers for High-Performance Organic Field-Effect Transistors. *Macromolecules* **2019**, *52* (12), 4765–4775. https://doi.org/10.1021/acs.macromol.9b00474.

(77) Zotti, G. Doping-Level Dependence of Conductivity in Polypyrroles and Polythiophenes. *Synthetic Metals* **1998**, *97* (3), 267–272. https://doi.org/10.1016/S0379-6779(98)00144-1.

(78) Zotti, G.; Zecchin, S.; Schiavon, G.; Groenendaal, L. "Bert." Conductive and Magnetic Properties of 3,4-Dimethoxy- and 3,4-Ethylenedioxy-Capped Polypyrrole and Polythiophene. *Chem. Mater.* **2000**, *12* (10), 2996–3005. https://doi.org/10.1021/cm000400l.

(79) Sannicolo, F.; Brenna, E.; Benincori, T.; Zotti, G.; Zecchin, S.; Schiavon, G.; Pilati, T. Highly Ordered Poly(Cyclopentabithiophenes) Functionalized with Crown-Ether Moieties for Lithium- and Sodium-Sensing Electrodes. 10.

(80) Zhu, S. S.; Swager, T. M. Conducting Polymetallorotaxanes: Metal Ion Mediated Enhancements in Conductivity and Charge Localization. *J. Am. Chem. Soc.* **1997**, *119* (51), 12568–12577. https://doi.org/10.1021/ja972794w.

(81) Welsh, D. M.; Kumar, A.; Meijer, E. W.; Reynolds, J. R. Enhanced Contrast Ratios and Rapid Switching in Electrochromics Based on Poly(3,4□ propylenedioxythiophene) Derivatives. 4.

(82) Color Control in π-Conjugated Organic Polymers for Use in Electrochromic.Pdf.

(83) Garreau, S.; Duvail, J. L.; Louarn, G. Spectroelectrochemical Studies of Poly(3,4-Ethylenedioxythiophene) in Aqueous Medium. *Synthetic Metals* **2001**, *125* (3), 325–329. https://doi.org/10.1016/S0379-6779(01)00397-6.

(84) Zozoulenko, I.; Singh, A.; Singh, S. K.; Gueskine, V.; Crispin, X.; Berggren, M. Polarons, Bipolarons, And Absorption Spectroscopy of PEDOT. *ACS Appl. Polym. Mater.* **2019**, *1* (1), 83–94. https://doi.org/10.1021/acsapm.8b00061.

(85) Yang, L.; Huang, X.; Gogoll, A.; Strømme, M.; Sjödin, M. Effect of the Linker in Terephthalate-Functionalized Conducting Redox Polymers. *Electrochimica Acta* **2016**, *222*, 149–155. https://doi.org/10.1016/j.electacta.2016.10.183.

(86) Åkerlund, L.; Emanuelsson, R.; Hernández, G.; Ruipérez, F.; Casado, N.; Brandell, D.; Strømme, M.; Mecerreyes, D.; Sjödin, M. In Situ Investigations of a Proton Trap Material: A PEDOT-Based Copolymer with Hydroquinone and Pyridine Side Groups Having Robust Cyclability in Organic Electrolytes and Ionic Liquids. *ACS Appl. Energy Mater.* **2019**, *2* (6), 4486–4495. https://doi.org/10.1021/acsaem.9b00735.

(87) Sterby, M.; Emanuelsson, R.; Huang, X.; Gogoll, A.; Strømme, M.; Sjödin, M. Characterization of PEDOT-Quinone Conducting Redox Polymers for Water Based Secondary Batteries. *Electrochimica Acta* **2017**, *235*, 356–364. https://doi.org/10.1016/j.electacta.2017.03.068.

(88) Huang, H.; Karlsson, C.; Strømme, M.; Gogoll, A.; Sjödin, M. Synthesis and Characterization of Poly-3-((2,5-Hydroquinone)Vinyl)-1H-Pyrrole: Investigation on Backbone/Pendant Interactions in a Conducting Redox Polymer. *Phys. Chem. Chem. Phys.* **2017**, *19* (16), 10427–10435. https://doi.org/10.1039/C6CP08736A.

(89) Yang, L.; Huang, X.; Mamedov, F.; Zhang, P.; Gogoll, A.; Strømme, M.; Sjödin, M. Conducting Redox Polymers with Non-Activated Charge Transport Properties. *Physical Chemistry Chemical Physics* **2017**, *19* (36), 25052–25058. https://doi.org/10.1039/C7CP03939E.

(90) Åkerlund, L.; Emanuelsson, R.; Hernández, G.; Ruipérez, F.; Casado, N.; Brandell, D.; Strømme, M.; Mecerreyes, D.; Sjödin, M. In Situ Investigations of a Proton Trap Material: A PEDOT-Based Copolymer with Hydroquinone and Pyridine Side Groups Having Robust Cyclability in Organic Electrolytes and Ionic Liquids. *ACS Appl. Energy Mater.* **2019**, *2* (6), 4486–4495. https://doi.org/10.1021/acsaem.9b00735.

(91) Strietzel, C.; Sterby, M.; Huang, H.; Strømme, M.; Emanuelsson, R.; Sjödin, M. An Aqueous Conducting Redox Polymer Based Proton Battery That Can Withstand Rapid Constant□voltage Charging and Sub□zero Temperatures. *Angew. Chem. Int. Ed.* **2020**, anie.202001191. https://doi.org/10.1002/anie.202001191.

(92) Huang, H.; Karlsson, C.; Strømme, M.; Gogoll, A.; Sjödin, M. Synthesis and Characterization of Poly-3-((2,5-Hydroquinone)Vinyl)-1H-Pyrrole: Investigation on Backbone/Pendant Interactions in a Conducting Redox Polymer. *Phys. Chem. Chem. Phys.* **2017**, *19* (16), 10427–10435. https://doi.org/10.1039/C6CP08736A.

(93) Emanuelsson, R.; Huang, H.; Gogoll, A.; Strømme, M.; Sjödin, M. Enthalpic versus Entropic Contribution to the Quinone Formal Potential in a Polypyrrole-Based Conducting Redox Polymer. *J. Phys. Chem. C* **2016**, *120* (38), 21178–21183. https://doi.org/10.1021/acs.jpcc.6b05353.

(94) Emanuelsson, R.; Sterby, M.; Strømme, M.; Sjödin, M. An All-Organic Proton Battery. *J. Am. Chem. Soc.* **2017**, *139* (13), 4828–4834. https://doi.org/10.1021/jacs.7b00159.

(95) Matching Diethyl Terephthalate with N□Doped Conducting Polymers.Pdf.

(96) Han, C.; Li, H.; Shi, R.; Zhang, T.; Tong, J.; Li, J.; Li, B. Organic Quinones towards Advanced Electrochemical Energy Storage: Recent Advances and Challenges. *J. Mater. Chem. A* **2019**, *7* (41), 23378–23415. https://doi.org/10.1039/C9TA05252F.

(97) Patil, N.; Mavrandonakis, A.; Jérôme, C.; Detrembleur, C.; Palma, J.; Marcilla, R. Polymers Bearing Catechol Pendants as Universal Hosts for Aqueous Rechargeable H^+, Li-Ion, and Post-Li-Ion (Mono-, Di-, and Trivalent) Batteries. *ACS Appl. Energy Mater.* **2019**, *2* (5), 3035–3041. https://doi.org/10.1021/acsaem.9b00443.

(98) Hui, Y.; Chng, E. L. K.; Chng, C. Y. L.; Poh, H. L.; Webster, R. D. Hydrogen-Bonding Interactions between Water and the One- and Two-Electron-Reduced Forms of Vitamin K_1: Applying Quinone Electrochemistry To Determine the Moisture Content of Non-Aqueous Solvents. *J. Am. Chem. Soc.* **2009**, *131* (4), 1523–1534. https://doi.org/10.1021/ja8080428.

(99) Wieland, M.; Malacrida, C.; Yu, Q.; Schlewitz, C.; Scapinello, L.; Penoni, A.; Ludwigs, S. Conductance and Spectroscopic Mapping of EDOT Polymer Films upon Electrochemical Doping. *Flex. Print. Electron.* **2020**, *5* (1), 014016. https://doi.org/10.1088/2058-8585/ab76e0.

(100) Zotti, G.; Zecchin, S.; Schiavon, G.; Groenendaal, L. "Bert." Conductive and Magnetic Properties of 3,4-Dimethoxy- and 3,4-Ethylenedioxy-Capped Polypyrrole and Polythiophene. *Chem. Mater.* **2000**, *12* (10), 2996–3005. https://doi.org/10.1021/cm000400l.

(101) Swager, T. M. *50th Anniversary Perspective* : Conducting/Semiconducting Conjugated Polymers. A Personal Perspective on the Past and the Future. *Macromolecules* **2017**, *50* (13), 4867–4886. https://doi.org/10.1021/acs.macromol.7b00582.

(102) Ayalew; Wang; Yu. Deprotonation-Induced Conductivity Shift of Polyethylenedioxythiophenes in Aqueous Solutions: The Effects of Side-Chain Length and Polymer Composition. *Polymers* **2019**, *11* (4), 659. https://doi.org/10.3390/polym11040659.

(103) Sheberla, D.; Patra, S.; Wijsboom, Y. H.; Sharma, S.; Sheynin, Y.; Haj-Yahia, A.-E.; Barak, A. H.; Gidron, O.; Bendikov, M. Conducting Polyfurans by Electropolymerization of Oligofurans. *Chem. Sci.* **2015**, *6* (1), 360–371. https://doi.org/10.1039/C4SC02664K.

(104) Ahonen, H. J.; Lukkari, J.; Kankare, J. N- and p-Doped Poly(3,4-Ethylenedioxythiophene): Two Electronically Conducting States of the Polymer. *Macromolecules* **2000**, *33* (18), 6787–6793. https://doi.org/10.1021/ma0004312.

(105) Swager, T. M. *50th Anniversary Perspective* : Conducting/Semiconducting Conjugated Polymers. A Personal Perspective on the Past and the Future. *Macromolecules* **2017**, *50* (13), 4867–4886. https://doi.org/10.1021/acs.macromol.7b00582.

(106) Strietzel, C.; Sterby, M.; Huang, H.; Strømme, M.; Emanuelsson, R.; Sjödin, M. An Aqueous Conducting Redox Polymer Based Proton Battery That Can Withstand Rapid Constant□voltage Charging and Sub□zero Temperatures. *Angew. Chem. Int. Ed.* **2020**, anie.202001191. https://doi.org/10.1002/anie.202001191.

(107) Olsson, H.; Sjödin, M.; Berg, E. J.; Strømme, M.; Nyholm, L. Self-Discharge Reactions in Energy Storage Devices Based on Polypyrrole-Cellulose Composite Electrodes. *Green* **2014**, *4* (1–6). https://doi.org/10.1515/green-2014-0003.

(108) Olsson, H.; Jämstorp Berg, E.; Strømme, M.; Sjödin, M. Self-Discharge in Positively Charged Polypyrrole–Cellulose Composite Electrodes. *Electrochemistry Communications* **2015**, *50*, 43–46. https://doi.org/10.1016/j.elecom.2014.11.004.

(109) Olsson, H.; Strømme, M.; Nyholm, L.; Sjödin, M. Activation Barriers Provide Insight into the Mechanism of Self-Discharge in Polypyrrole. *J. Phys. Chem. C* **2014**, *118* (51), 29643–29649. https://doi.org/10.1021/jp510690p.

(110) Zykwinska, A.; Domagala, W.; Pilawa, B.; Lapkowski, M. Electrochemical Overoxidation of Poly(3,4-Ethylenedioxythiophene)—PEDOT Studied by Means of in Situ ESR Spectroelectrochemistry. *Electrochimica Acta* **2005**, *50* (7–8), 1625–1633. https://doi.org/10.1016/j.electacta.2004.10.026.

(111) Takano, T.; Masunaga, H.; Fujiwara, A.; Okuzaki, H.; Sasaki, T. PEDOT Nanocrystal in Highly Conductive PEDOT:PSS Polymer Films. *Macromolecules* **2012**, *45* (9), 3859–3865. https://doi.org/10.1021/ma300120g.
(112) Baik, W.; Luan, W.; Zhao, R. H.; Koo, S.; Kim, K.-S. Synthesis of Highly Conductive Poly(3,4-Ethylenedioxythiophene) Fiber by Simple Chemical Polymerization. *Synthetic Metals* **2009**, *159* (13), 1244–1246. https://doi.org/10.1016/j.synthmet.2009.02.044.

Acta Universitatis Upsaliensis

Digital Comprehensive Summaries of Uppsala Dissertations from the Faculty of Science and Technology 1972

Editor: The Dean of the Faculty of Science and Technology

A doctoral dissertation from the Faculty of Science and Technology, Uppsala University, is usually a summary of a number of papers. A few copies of the complete dissertation are kept at major Swedish research libraries, while the summary alone is distributed internationally through the series Digital Comprehensive Summaries of Uppsala Dissertations from the Faculty of Science and Technology. (Prior to January, 2005, the series was published under the title "Comprehensive Summaries of Uppsala Dissertations from the Faculty of Science and Technology".)

Distribution: publications.uu.se
urn:nbn:se:uu:diva-419470

ACTA
UNIVERSITATIS
UPSALIENSIS
UPPSALA
2020